
# The Galactic Center arms inferred from the ALMA CMZ Exploration Survey (ACES)

*Publications of the Astronomical Society of Japan*, 2025, **77**(4), 687–706
https://doi.org/10.1093/pasj/psaf034
Advance access publication date: 2025 June 11

# The Galactic Center arms inferred from the ALMA CMZ Exploration Survey (ACES)

**Yoshiaki Sofue,[1,*] Tomoharu Oka,[2] Steven N. Longmore,[3,4] Daniel Walker,[5] Adam Ginsburg,[6] Jonathan D. Henshaw,[3,7] John Bally,[8] Ashley T. Barnes,[9] Cara Battersby,[10] Laura Colzi,[11] Paul Ho,[12] Izaskun Jimenez-Serra,[11] J. M. Diederik Kruijssen,[4,13] Elizabeth Mills,[14] Maya A. Petkova,[15] Mattia C. Sormani,[16,17] Jen Wallace,[10] Jairo Armijos-Abendaño,[18] Katarzyna M. Dutkowska,[19] Rei Enokiya,[20] Yasuo Fukui,[21] Pablo García,[22,23] Andres Guzman,[24] Christian Henkel,[25] Pei-Ying Hsieh,[26] Yue Hu,[27] Katharina Immer,[9] Desmond Jeff,[6,28] Ralf S. Klessen,[29,30,31,32] Kotaro Kohno,[1] Mark R. Krumholz,[33] Dani Lipman,[10] Mark R. Morris,[34] Francisco Nogueras-Lara,[9] M. Nonhebel,[9,35] Jürgen Ott,[36] Jaime E. Pineda,[37] Sergio Martín,[38,39] Miguel Angel Requena-Torres,[40] Víctor M. Rivilla,[11] Denise Riquelme-Vásquez,[41] Álvaro Sánchez-Monge,[42,43] Miriam G. Santa-Maria,[6] Howard A. Smith,[31] Tabassum S. Tanvir,[44] Volker Tolls,[31] and Q. Daniel Wang[45]**

[1]Institute of Astronomy, The University of Tokyo, 2-21-1 Osawa, Mitaka, Tokyo 181-0015, Japan
[2]Department of Physics, Faculty of Science and Technology, Keio University, 3-14-1 Hiyoshi, Yokohama, Kanagawa 223-8522, Japan
[3]Astrophysics Research Institute, Liverpool John Moores University, IC2, Liverpool Science Park, 146 Brownlow Hill, Liverpool L3 5RF, UK
[4]Cosmic Origins Of Life (COOL) Research DAO, https://coolresearch.io
[5]UK ALMA Regional Centre Node, Jodrell Bank Centre for Astrophysics, The University of Manchester, Oxford Road, Manchester M13 9PL, UK
[6]Department of Astronomy, University of Florida, PO Box 112055, Gainesville, FL 32611, USA
[7]Max Planck Institute for Astronomy, Königstuhl 17, D-69117 Heidelberg, Germany
[8]Center for Astrophysics and Space Astronomy, Department of Astrophysical and Planetary Sciences, University of Colorado, Boulder, CO 80389, USA
[9]European Southern Observatory (ESO), Karl-Schwarzschild-Strasse 2, D-85748 Garching, Germany
[10]Department of Physics, University of Connecticut, 196A Auditorium Road, Unit 3046, Storrs, CT 06269, USA
[11]Centro de Astrobiología (CAB), CSIC-INTA, Carretera de Ajalvir km 4, Torrejón de Ardoz, E-28850 Madrid, Spain
[12]AS/NTU Astronomy-Mathematics Building, Roosevelt Rd, Taipei 10617, Taiwan
[13]Technical University of Munich, School of Engineering and Design, Department of Aerospace and Geodesy, Arcisstr. 21, D-80333 Munich, Germany
[14]Department of Physics and Astronomy, University of Kansas, 1251 Wescoe Hall Drive, Lawrence, KS 66045, USA
[15]Space, Earth and Environment Department, Chalmers University of Technology, SE-412 96 Gothenburg, Sweden
[16]Università dell'Insubria, via Valleggio 11, I-22100 Como, Italy
[17]Department of Physics, University of Surrey, Guildford GU2 7XH, UK
[18]Observatorio Astronómico de Quito, Observatorio Nacional, Escuela Politécnica Nacional, Interior del Parque La Alameda, 170136 Quito, Ecuador
[19]Leiden Observatory, Leiden University, PO Box 9513, NL-2300 RA Leiden, the Netherlands
[20]Department of Physics, Nagoya University, Furo-cho, Chikusa-ku, 464-8602, Japan
[21]Department of Physics, Nagoya University, Chikusa-ku, Nagoya 464-8602, Japan
[22]Chinese Academy of Sciences South America Center for Astronomy, National Astronomical Observatories, CAS, Beijing 100101, China
[23]Instituto de Astronomía, Universidad Católica del Norte, Av. Angamos 0610, Antofagasta, Chile
[24]Joint ALMA Observatory, Alonso de Cordova 3107, Vitacura 763-0355, Santiago de Chile, Chile
[25]MPIfR, Auf dem Hügel 69, D-53121 Bonn, Germany
[26]National Astronomical Observatory of Japan, 2-21-1 Osawa, Mitaka, Tokyo 181-8588, Japan
[27]Institute for Advanced Study, 1 Einstein Drive, Princeton, NJ 08540, USA
[28]National Radio Astronomy Observatory, 520 Edgemont Road, Charlottesville, VA 22903, USA
[29]Universität Heidelberg, Zentrum für Astronomie, Institut für Theoretische Astrophysik, Albert-Ueberle-Str. 2, D-69120 Heidelberg, Germany
[30]Universität Heidelberg, Interdisziplinäres Zentrum für Wissenschaftliches Rechnen, Im Neuenheimer Feld 225, D-69120 Heidelberg, Germany
[31]Center for Astrophysics, Harvard & Smithsonian, 60 Garden Street, Cambridge, MA 02138, USA
[32]Elizabeth S. and Richard M. Cashin Fellow at the Radcliffe Institute for Advanced Studies at Harvard University, 10 Garden Street, Cambridge, MA 02138, USA
[33]Research School of Astronomy and Astrophysics, Australian National University, Cotter Road, Weston, ACT 2611, Australia

**Received:** 2024 November 7; **Accepted:** 2025 March 25

[34]Department of Physics and Astronomy, University of California, Los Angeles, CA 90095, USA
[35]SUPA, School of Physics and Astronomy, University of St Andrews, North Haugh, St. Andrews, KY16 9SS, UK
[36]National Radio Astronomy Observatory, PO Box O, 1011 Lopezville Road, Socorro, NM 87801, USA
[37]MPI for Extraterrestrial Physics, Giessenbachstr. 1, D-85748, Garching by München, Germany
[38]European Southern Observatory, Alonso de Córdova, 3107, Vitacura, Santiago 763-0355, Chile
[39]Joint ALMA Observatory, Alonso de Córdova, 3107, Vitacura, Santiago 763-0355, Chile
[40]Department of Physics, Astronomy, and Geosciences, Towson University, Towson, MD 21252, USA
[41]Departamento de Astronomía, Universidad de La Serena, Raúl Bitrán 1305, La Serena, Chile
[42]Institut de Ciències de l'Espai (ICE), CSIC, Campus UAB, Carrer de Can Magrans s/n, E-08193 Bellaterra (Barcelona), Spain
[43]Institut d'Estudis Espacials de Catalunya (IEEC), E-08860 Castelldefels (Barcelona), Spain
[44]Department of Physics and Astronomy, Iowa State University, 2323 Osborn Drive, Ames, IA 50010, USA
[45]Department of Astronomy, University of Massachusetts, Amherst, MA 01003, USA
*E-mail: sofue@ioa.s.u-tokyo.ac.jp

## Abstract

Analyzing longitude–velocity diagrams (LVDs) in the CS ($J = 2$–1) and H$^{13}$CN ($J = 1$–0) molecular lines from the internal release data of the ALMA Central Molecular Zone (CMZ) Exploration Survey and in the $^{13}$CO ($J = 1$–0) line from the Nobeyama Galactic Center (GC) survey, we identify six GC arms as prominent straight LV ridges. In addition to the currently known Arms I to IV, we identify a new inner arm, Arm V, and further highlight the circumnuclear disk (CND) as Arm VI. Integrated intensity maps of the arms on the sky suggest that most of the arms compose ring-like structures inclined from the Galactic plane. We determine the radii (curvatures) of the arms using the velocity-gradient ($dv/dl$) method, assuming that the arms are rotating in circular orbits at a constant velocity of ∼150 km s$^{-1}$. We show that Arms I and II compose the main ring structure of the CMZ with radii ∼100–120 pc; Arm III is a dense arm 42 pc from the GC; Arm IV is a clear and narrow arm 20 pc from the GC; and Arm V is a faint, long arm of 8.2 pc radius. We show that the CND comprises the sixth arm, Arm VI, of radius ∼2.3 pc associated with bifurcated spiral fins. We also discuss the association of the 20 and 50 km s$^{-1}$ clouds with these arms. The radii of the arms fall on an empirical relation $R \sim 630(2/5)^N$ for $N = 1$ (Arm I) to 6 (VI), suggesting discrete rings or a logarithmic spiral with pitch angle ∼22°. The vertical full extent of the arm increases with radius and is represented by $z \sim 0.7(R/1\ \mathrm{pc})^{0.7}$ pc. The tilt angle of the arms from the Galactic plane, or the warping, increases rapidly toward the GC.

**Keywords:** Galaxy: Center — Galaxy: structure — ISM: clouds — ISM: molecules — ISM: kinematics and dynamics

## 1 Introduction

Because we see the Galactic Central Molecular Zone (CMZ) edge-on, its true 3D structure is challenging to decipher and remains substantially uncertain (Morris & Serabyn 1996; Henshaw et al. 2016, 2023; Sofue 2022). Kinematic analysis of longitude–velocity diagrams (LVDs), assuming Galactic rotation, offers one way to help to resolve line-of-sight degeneracy (Bally et al. 1987, 1988; Sofue 1995, 2022; Oka et al. 1998; Tsuboi et al. 1999; Kruijssen et al. 2015; Henshaw et al. 2016, 2023). Here, we exploit the special behavior of a rotating arm or a ring in the longitude–velocity diagram (LVD), which makes the LV ridge appear sharpest near its intersection with the rotation axis at $l \sim 0°$. The absorption of line emission against the background continuum helps to distinguish the far and near sides of clouds relative to Sgr A* (Sawada et al. 2004; Yan et al. 2017; Sofue 2022).

The coherent ridges on the LVD suggest that the CMZ is structured into multiple arms. The densest and most prominent LV ridge seen in the $^{13}$CO ($J = 1$–0) line is called Galactic Center (GC) Arm I, the second is Arm II, and further arms (III and IV) have been proposed (Sofue 1995). There seems to be consensus that Arms I and II compose a ring structure of radius ∼100–120 pc (the "120 pc ring") (Sofue 1995; Oka et al. 1998; Henshaw et al. 2016, 2023; Tokuyama et al. 2019), which is understood as being due to a large-scale accretion of gas from the outer Galactic disk (Molinari et al. 2011; Kim & Stone 2012; Kruijssen et al. 2015; Krumholz & Kruijssen 2015; Krumholz et al. 2017; Ridley et al. 2017; Sormani et al. 2019, 2020; Tress et al. 2020).

However, the more internal structure of molecular gas within the CMZ inside the 120 pc ring appears to have not yet been fully explored but is believed to consist of a continuous disk, arms/rings or a hole (empty space), or a combination of these. Among these, the arm/ring structure can be most easily recognized using high-resolution molecular-line mapping data, while the other structures may be obtained as the residual. For the purpose of mapping arms/rings of molecular gas, we analyze the data cubes observed with the Nobeyama 45 m telescope in the $^{13}$CO ($J = 1$–0) line, ASTE (Atacama Submm Telescope Experiments) 10 m telescope in HCN ($J = 4$–3), and ALMA (Atacama Large Millimeter/submillimeter Array) in the course of the large project ACES (ALMA CMZ Exploration Survey) in the CS ($J = 2$–1) and H$^{13}$CN ($J = 1$–0) lines (ALMA Program, 2021.1.00172.L; PI: S. Longmore et al. in preparation). Thanks to the high spatial resolution offered by ALMA, we can greatly improve arm identification at the very center inside $|l| \lesssim 0.^\circ2$ (∼30 pc).

The region around Sgr A* contains many well known molecular clouds including the 50 km s$^{-1}$ cloud (hereafter 50 kmC) and 20 km s$^{-1}$ cloud (20 kmC) (Genzel et al. 1990; Tsuboi et al. 2009), high-velocity compact clouds (HVCCs) (Oka et al. 1999; Iwata et al. 2023), the circumnuclear disk (CND) (Wright et al. 2001; Tsuboi et al. 2018), and the mini-spirals around Sgr A* (Tsuboi et al. 2017). We try to understand these innermost structures under a unified view of a molecular disk with arms/rings rapidly rotating in the deep gravitational potential that reaches specific kinetic energies of $\sim V_{\rm rot}^2/2 \sim 10^{14}$ erg g$^{-1}$ at $V_{\rm rot} \sim 100$–150 km s$^{-1}$.

In this study, we combine $^{13}$CO ($J = 1$–0) and HCN ($J = 4$–3) single-dish data with the ACES interferometric mosaics in CS ($J = 2$–1) and H$^{13}$CN ($J = 1$–0) at $|l| \lesssim 0.^\circ2$ to determine the internal kinematical structure of the CMZ by constraining the radii and vertical extents of the arms/rings present within ∼100 pc. This will help us to visualize the gaseous structure in the circumnuclear region, which is essential to carry out the 3D modeling of the CMZ.

We adopt a solar galactocentric distance $R_0 = 8.2$ kpc, close to the recent measurement (Gravity Collaboration 2019), for convenience to compare with the other works. The coordinates of Sgr A* are taken to be $(l, b) = (359.^\circ944227, -0.^\circ046157) = (359^\circ56'39.''2, -00^\circ02'46.''2)$, and the LSR (local standard of rest) velocity is assumed to be $v_{\rm LSR} = 0$ km s$^{-1}$.

## 2 Data and analysis

### 2.1 Single-dish data

We used the archival data cube of the $^{13}$CO ($J = 1$–0) line emission at 110.27 GHz taken from the CMZ survey obtained using the Nobeyama 45 m telescope (Tokuyama et al. 2019). The data cube had sampling grids of ($7.''5 \times 7.''5 \times 2$ km s$^{-1}$) with an effective resolution of $16.''7$, which yielded an rms noise of $\sim$0.15 K in brightness temperature, $T_{\rm B}$. We also used an archival data cube of the HCN ($J = 4$–3) line emission at 354.5 GHz from the GC survey with the ASTE 10 m telescope (Tanaka et al. 2018), which had ($8.''5 \times 8.''5 \times 2$ km s$^{-1}$) grids with an effective angular resolution of $24''$ and rms noise of 0.14 K in $T_{\rm B}$.

### 2.2 ACES

The molecular-line cubes from ALMA used in this work were taken from the internal release version of the 12 m + 7 m + TP (total power)-mode data from the ALMA cycle 8 Large Program "ALMA Central Molecular Zone Exploration Survey" (ACES, 2021.1.00172.L; S. Longmore et al. in preparation). ACES observed the CMZ in ALMA Band 3, covering a frequency range of $\sim$86–101 GHz across six spectral windows of varying spectral resolution and bandwidth.

The ALMA pipeline calibrated measurement sets were produced using CASA 6.4.1.12, and all of the 12 m and 7 m data were reimaged using CASA 6.4.3-2. In general, the imaging parameters were the same as those used by the pipeline to produce the delivered data, but there were instances where parameters were changed, in particular to fix divergent channels, and to undo size mitigation performed by the default pipeline parameters.

We also found that the ALMA pipeline often did not perform optimally when identifying line-free channels in the data, resulting in residual continuum emission after the continuum subtraction. The pipeline also used a polynomial fit order of 1, which often resulted in poor baselines after continuum subtraction, particularly in the narrow spectral windows, which are often filled with broad line emission. To fix these issues, we first reran the continuum subtraction using a fit order of 0, and then additionally used `statcont` (Sánchez-Monge et al. 2018) to remove the residual continuum emission. After reimaging and subtracting the continuum, we combined the 12 m, 7 m, and TP data using the `feather` task in CASA. We first combined the 7 m and TP cubes, then combined this 7 m + TP cube with the 12 m data.

The ACES coverage is split into 45 individual sub-mosaics, each with approximately 150 pointings. For each line/spectral window (SPW), we used the `radio-beam` and `reproject` Python packages to convolve all sub-mosaics to a common beam, and then project them on to the full ACES footprint. The resulting cubes provide a contiguous mosaic of the CMZ.

For this work, we used the cubes in the CS ($J = 2$–1) line at a frequency of 97.9810 GHz with FWHM angular resolution $2.''21$ of the synthesized beam and rms noise of 0.0038 Jy beam$^{-1}$ (0.10 K) with velocity channel increments of 1.45 km s$^{-1}$, and the H$^{13}$CN ($J = 1$–0) line at 86.3399 GHz with resolution $2.''72$ and rms noise 0.0046 Jy beam$^{-1}$ (0.10 K) with velocity channel increments of 0.88 km s$^{-1}$. The intensity scales are Jy beam$^{-1}$ (1 Jy beam$^{-1}$ = 26.1 and 22.2 K in brightness temperature at 98 and 86 GHz, respectively).

The cubes cover the CMZ at $-0.^\circ6 \lesssim l \lesssim +0.^\circ9$ and $-0.^\circ3 \lesssim b \lesssim +0.^\circ1$, and the velocity ranges were $-220 \le v_{\rm LSR} \le +220$ km s$^{-1}$ and $-150 \le v_{\rm LSR} \le +150$ km s$^{-1}$, respectively, with spatial and velocity grids of ($0.''5 \times 0.''5 \times 0.15$ km s$^{-1}$). We further cut out a more interior region at $-0.^\circ25 \le l \le +0.^\circ15$ and $-0.^\circ1 \le b \le +0^\circ$ for a detailed analysis of the circumnuclear region centered on Sgr A*.

### 2.3 Definition and identification of the arms

The goal of this paper is to identify spiral arms, rings, and/or segments thereof (hereafter "arms") in the CMZ that rotate within the Galactic gravitational potential, and to quantify their galactocentral radii or curvatures. An "arm" is here defined by a tilted ridge on the LVD that extends straight for $\sim\pm$100 km s$^{-1}$, indicating a coherent ring-like structure rotating at $\sim$100–150 km s$^{-1}$.

We used the $^{13}$CO ($J = 1$–0) line from the single dish in order to trace the arms and extended structure in the entire CMZ. The lines CS ($J = 2$–1) and H$^{13}$CN ($J = 1$–0) from the ALMA cubes were chosen to trace the innermost arms, which are supposed to consist of relatively denser molecular gas (Shirley 2015), for a complementary analysis to the $^{13}$CO ($J = 1$–0) line from the single dish.

To identify the arms, we exploit a special property of the LVD that, due to the degeneracy of the radial velocity, the arms appear clearest and brightest near their intersection with the axis of rotation at $l \sim 0^\circ$. Although some arms overlap at $l \sim 0^\circ$, they can be distinguished from one another because their ridges run at different tilt angles (Sofue 2006). Moreover, fortunately, non-circular motions overlap in most spiral arms, which yields displacements of $v_{\rm LSR}$ from zero near $l \sim 0^\circ$, so in most cases the degeneracy is resolved, or the LV ridges do not overlap at the intersection point.

Note that there are four ways to display LVD as follows.

Type 1: channel LVD at every latitude as one channel of the cube;

Type 2: total average over all latitudes;

Type 3: average over selected latitudes; and

Type 4: LVD, maximum intensity (peak $T_{\rm B}$) across latitudes.

They are all used in this work depending on the purpose of each figure.

However, especially in the central region, the LV arms are often buried in bright extended features. In order to abstract such buried arms by subtracting more extended structures, we apply the IMSHIFT-relieving technique described in appendix 1. This method is particularly useful for the single-dish data with lower angular resolution.

By tracing the tilted LVD ridge (LVR), we measure the longitudinal velocity gradient $dv/dl$, which is related to the radius or curvature of the arm as explained in detail in subsection 4.1. For identifying a spiral arm or a ring, this method is more sensitive and accurate than measuring the terminal velocity ends at the farthest longitudes, because the inherent width and velocity dispersion make it difficult to define the exact terminal longitude and velocity.

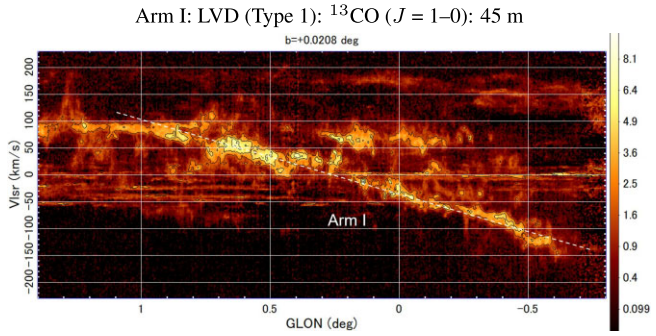


**Fig. 1.** Longitude–velocity diagram (LVD) showing the Galactic Center (GC) Arm I in $^{13}$CO ($J = 1$–0) from the 45 m telescope at a representative latitude (Type-1 LVD). Color bars indicate the brightness temperature in K.

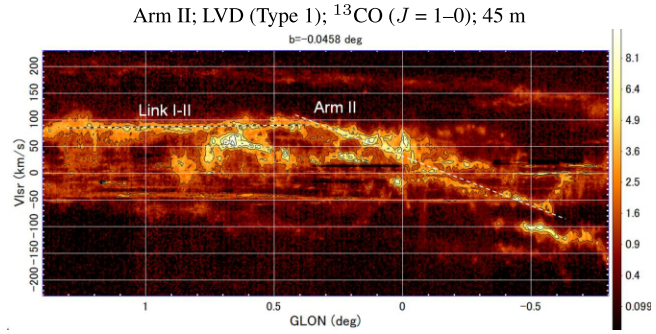


**Fig. 2.** Arm II on the LVD in $^{13}$CO ($J = 1$–0) from the 45 m telescope at a representative latitude that is indicated in each panel. The horizontal line labeled Link I–II indicates the possible connection of Arm II with Arm I as well as with the outer disk. Color bars indicate the brightness temperature in K.

## 2.4 LVD "arms"

We search for arms in all channels of the cubes as LV ridges with extents over ±100 km s$^{-1}$. In figures 1–6 we show the LVDs at representative latitudes of the thus-recognized GC arms in the $^{13}$CO ($J = 1$–0) line from Nobeyama 45 m, HCN ($J = 4$–3) from ASTE 10 m, and CS ($J = 2$–1) and H$^{13}$CN ($J = 1$–0) from ALMA. Details of the data are shown in individual panels of the figures and captions. The identified arms are marked by white dashed lines or arrows with the corresponding names.

The arms are often too thin and faint to be recognized on a single or on averaged LVD. In order to convincingly trace such arms in more detail, we also use channel LVDs as presented in appendix 2.

In figure 7 we summarize all the the arms identified by dashed lines superposed on the maximum intensity LVD from ALMA in the whole mapped area by ACES in CS ($J = 2$–1) from $b = -0.^{\circ}3$ to $+0.^{\circ}2$. The middle and bottom panels show the same in CS ($J = 2$–1) and H$^{13}$CN ($J = 1$–0), but for the central region from $l = -0.^{\circ}25$ to $0.^{\circ}15$, and $b = -0.^{\circ}1$ to $0^{\circ}$. These LVDs were made by creating maximum-intensity projections along the latitude axis of the cubes using the `spectral-cube` Python package.

## 2.5 Vertical profiles of the arms

Figure 8 shows the latitudinal intensity profiles of the arms averaged along the LV ridges of the individual arms inside the red boxes as shown in the LVD inset in each panel. We then

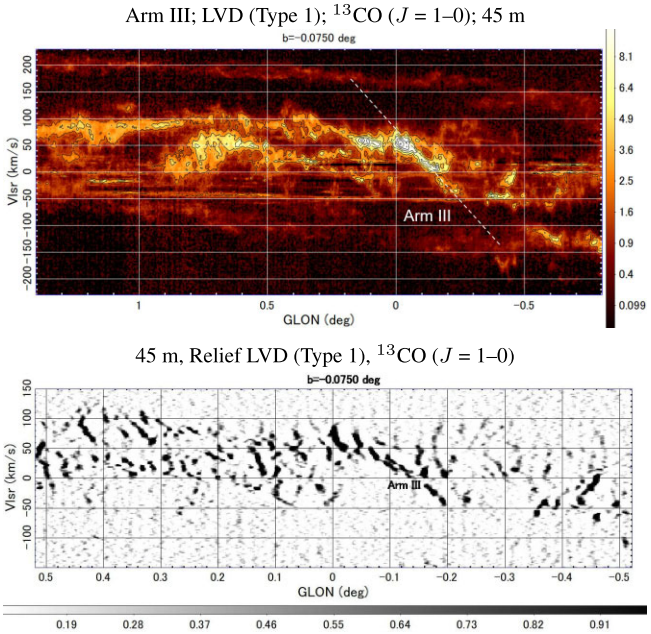


**Fig. 3.** [Top] Arm III LVD in $^{13}$CO ($J = 1$–0) from the 45 m telescope at representative latitude $b = -0.^{\circ}075$. [Bottom] Same, but relieved LVD (see appendix 1 for the relieving method) for the central region. Color bars indicate the brightness temperature in K.

measure the full width at half maximum (FWHM) of the profile, as indicated by the red arrow, and define the width as the "$z$ = full vertical extent" of the arm. The bottom-right image explains the procedure for obtaining the latitudinal profile of an arm.

The full-width vertical extents of the arms are thus obtained to be $z \sim 27.2$ pc for Arm I, ∼22.9 pc for Arm II, ∼12.9–5.7 pc for Arm III in $^{13}$CO ($J = 1$–0) and CS ($J = 2$–1), respectively, ∼4.3 pc for Arm IV, ∼3.1–3.3 pc for Arm V in $^{13}$CO ($J = 1$–0) and CS ($J = 2$–1), and ∼1.3 pc for Arm VI (CND). We find that the vertical extent of the arms decreases from Arm I to VI; this will be discussed in subsection 4.1. The derived quantities are listed in table 1.

## 2.6 Arms on the sky (moment-0 maps along LV ridges): The LV-masking method

We then produce integrated intensity (moment-0) maps around the LV ridges of Arms I to VI (CND) indicated by the dashed lines in the LVDs in figures 1–7, using "masked cube" created by convolving the original cube with a cube of the same size (masking cube) representing a Gaussian function, or the "LV-masking function,"

$$f(l, v_{\rm LSR}) = \exp\left[-\left(\frac{v_{\rm LSR} - v_{\rm ridge}(l)}{\delta v}\right)^2\right]. \quad (1)$$

Here, $v_{\rm ridge}(l)$ represents $v_{\rm LSR}$ of the LV ridge at longitude $l$, and is expressed by a linear or bent-linear (curved) function of $l$ to represent the dashed line of each arm in figures 1–7. So, in most cases,

$$v_{\rm ridge}(l) = Al + B, \quad (2)$$

where $A = dv_{\rm LSR}/dl$ and $B = v_{l=0^{\circ}}$ and are taken to be constants, and were measured along each of the dashed lines

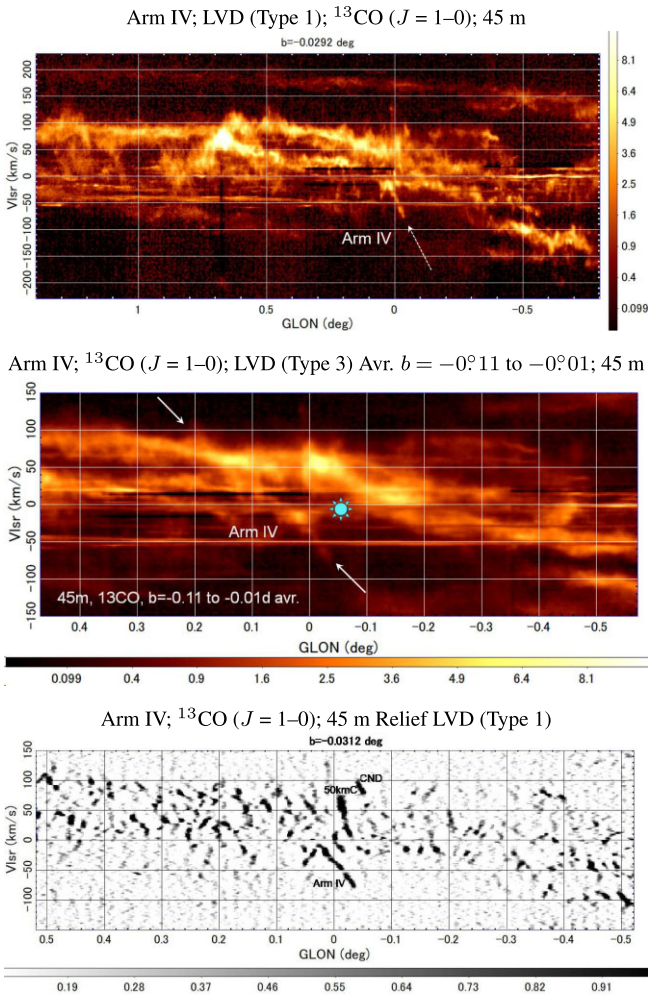


**Fig. 4.** Arm IV: [Top] LVD (Type 1) in $^{13}$CO ($J = 1$–0) from the 45 m telescope at representative latitude $b = -0.^{\circ}03$. [Middle] LVD averaged between $b = 0.^{\circ}11$ and $-0.^{\circ}01$ (Type-3 LVD), showing the entire arm including positive-velocity extensions. [Bottom] Relieved LVD (Type 1) at $b = -0.^{\circ}03$, showing the negative velocity ridge. Color bars indicate the brightness temperature in K. The blue symbol is Sgr A*.

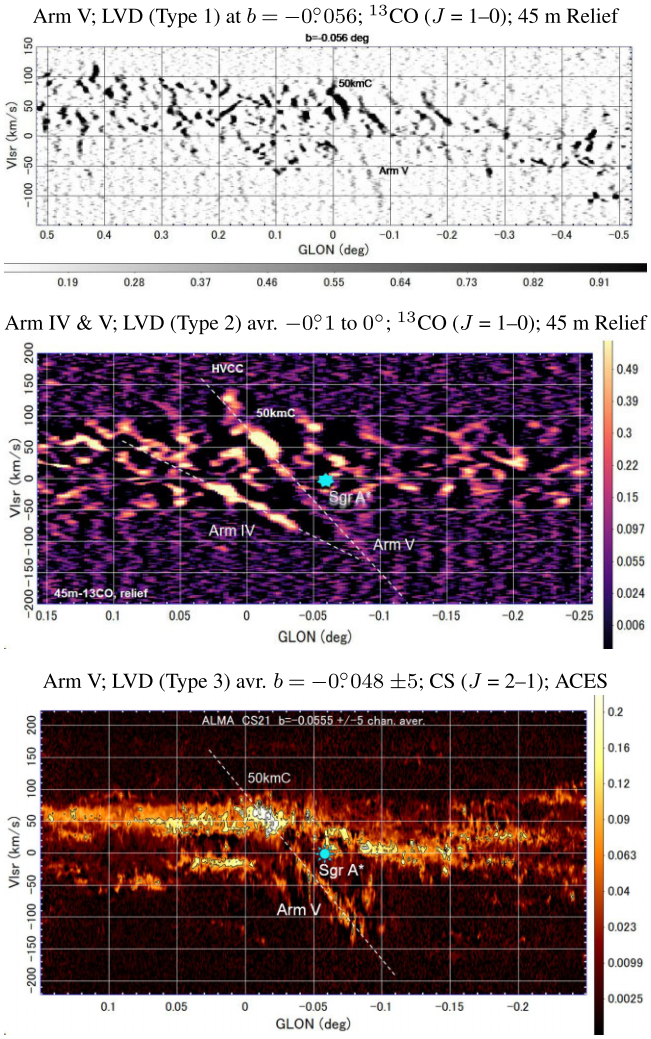


**Fig. 5.** Arm V: [Top] Releaved LVD (Type 1) in $^{13}$CO ($J = 1$–0) from the 45 m telescope at representative latitude $b = -0.^{\circ}056$. [Bottom] LVD (Type 3) in CS ($J = 2$–1) averaged over $\pm 5$ ($\pm 4$ km s$^{-1}$) channels around $b = -0.^{\circ}0555$ by ALMA. [Middle] Relieved LVD (Type 3) in $^{13}$CO ($J = 1$–0) averaged between $-0.^{\circ}1$ and $0^{\circ}$.

in figures 1–7. The velocity half width was estimated to be $\delta v = 10$ and 7.5 km s$^{-1}$ for $^{13}$CO ($J = 1$–0) and CS ($J = 2$–1), respectively, using LVDs around the clearest parts of Arms I to III (figures 1–3) and Arms IV and V (figures 4 and 5).

The moment-0 maps obtained along the LV ridges from the 45 m telescope in $^{13}$CO ($J = 1$–0) and from ALMA in CS ($J = 2$–1) and H$^{13}$CN ($J = 1$–0) are shown in figures 9 and 10, respectively. The vertical broad and bright bands in the maps of Arms IV to VI from ALMA are contaminations of the local disk and the "fore-/background CMZ" including part of Arms I and II.

## 3 Galactic Center arms

The so-far-identified Arms I to VI are summarized in the LVD of figure 7 by the dashed lines. In this section we describe the individual arms based on the LVDs as well as the LV-masked moment-0 maps. We highlight the inner Arms III and IV and report the existence of a new arm, which we name Arm V. We further identify an even inner arm, naming it Arm VI, which is an alternate view of the CND (Wright et al. 2001; Tsuboi et al. 2018). We also discuss the mini-spirals around Sgr A* (Tsuboi et al. 2017), which we consider to be the innermost family of the arms and thus call Arm VII.

### 3.1 Arm I

Arm I, or the Sgr-B arm, appears as the most prominent LV ridge of the CMZ, and is considered to be a spiral arm or a ring on the nearer side of Sgr A*, the Milky Way's nucleus. Moment-0 maps of this arm shown in panels (A) and (B) of figure 9 reveal a long and sharp arm tailing from the Sgr B cloud complex. The active star-forming regions Sgr B1 and B2 are located in this arm (Sofue 1995, 2022; Oka et al. 1998; Henshaw et al. 2016, 2023; Tokuyama et al. 2019).

### 3.2 Arm II

Arm II, or the Sgr-C arm, is the second-brightest arm associated with Sgr C, and is rotating on the far side of Sgr A. Arms I and II are linked by a horizontal LV belt (Link I–II), as indicated by the dashed line in figure 7.

Link I–II appears to be connected to the disk further out at velocities at $v_{\rm LSR} \sim 100$ km s$^{-1}$, which may suggest a gaseous arm connecting the CMZ and the Galactic disk. However, we

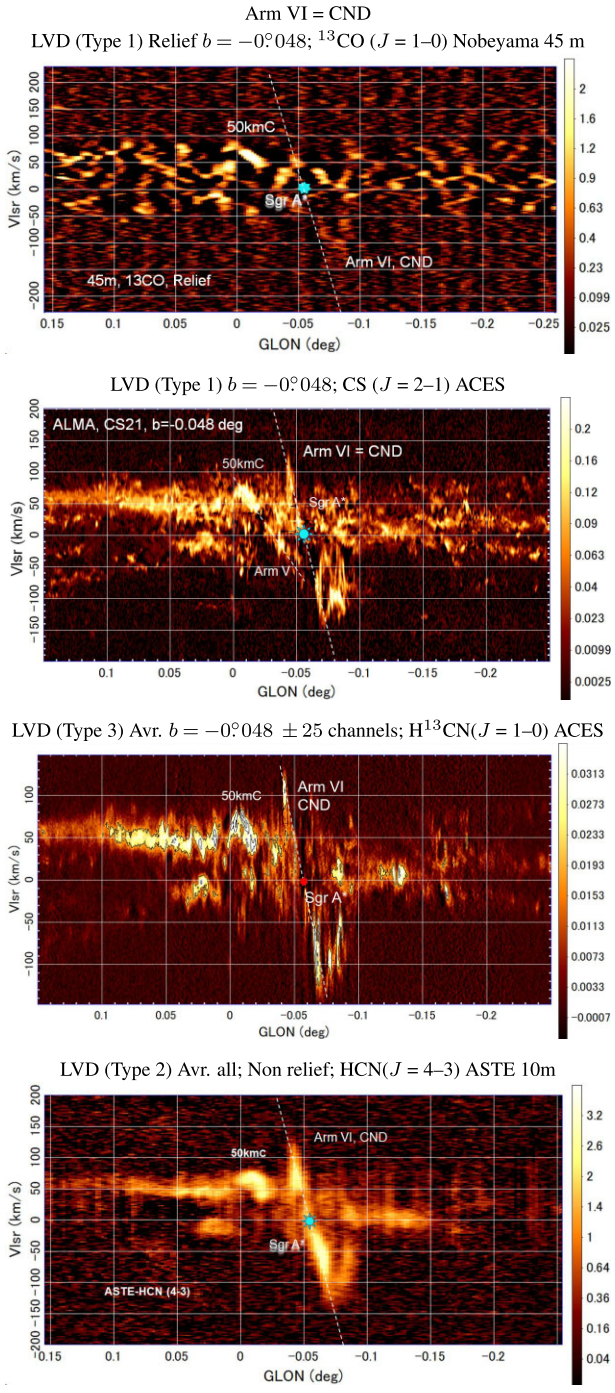


**Fig. 6.** Arm VI: [Top] 45 m LVD (Type 1, relief) in $^{13}$CO ($J$ = 1–0) at $b = -0.^{\circ}048$. [2nd] ALMA CS ($J$ = 2–1) LVD (Type 1) from ACES internal release data. [3rd] ALMA H$^{13}$CN ($J$ = 1–0) LVD (Type 3). [Bottom] ASTE H$^{13}$CN ($J$ = 1–0) LVD (Type 2) averaged over all latitudes. Color bars indicate the brightness temperature in K for the top panel (45 m), and in Jy beam$^{-1}$ for the others (ACES).

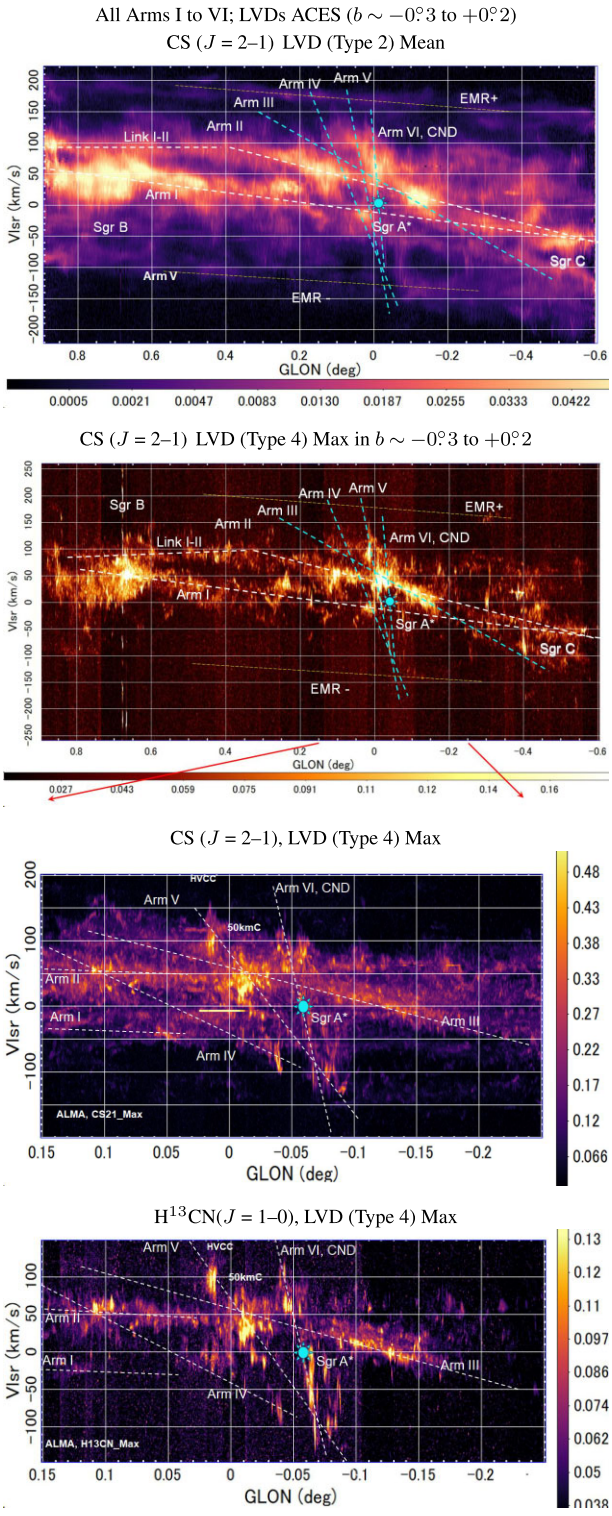


**Fig. 7.** [Top] LVD of latitudinal mean CS ($J$ = 2–1) intensity. The identified arms are indicated by the dashed lines. EMR stands for expanding molecular ring (+/- for positive and negative $v_{LSR}$, respectively). [2nd] LVD of maximum (peak) intensity along each latitude in CS ($J$ = 2–1). Arm III shows up clearly in this map. [3rd] Same, but the central region. [Bottom] Same, but in H$^{13}$CN ($J$ = 1–0). Color bars indicate the intensity scale in Jy beam$^{-1}$.

do not discuss this feature in this paper, because it is far outside the ACES field.

In panel (C) of figure 9 we show a moment-0 map integrated along the bent LVR Arm II and Link I–II (figure 2). This map

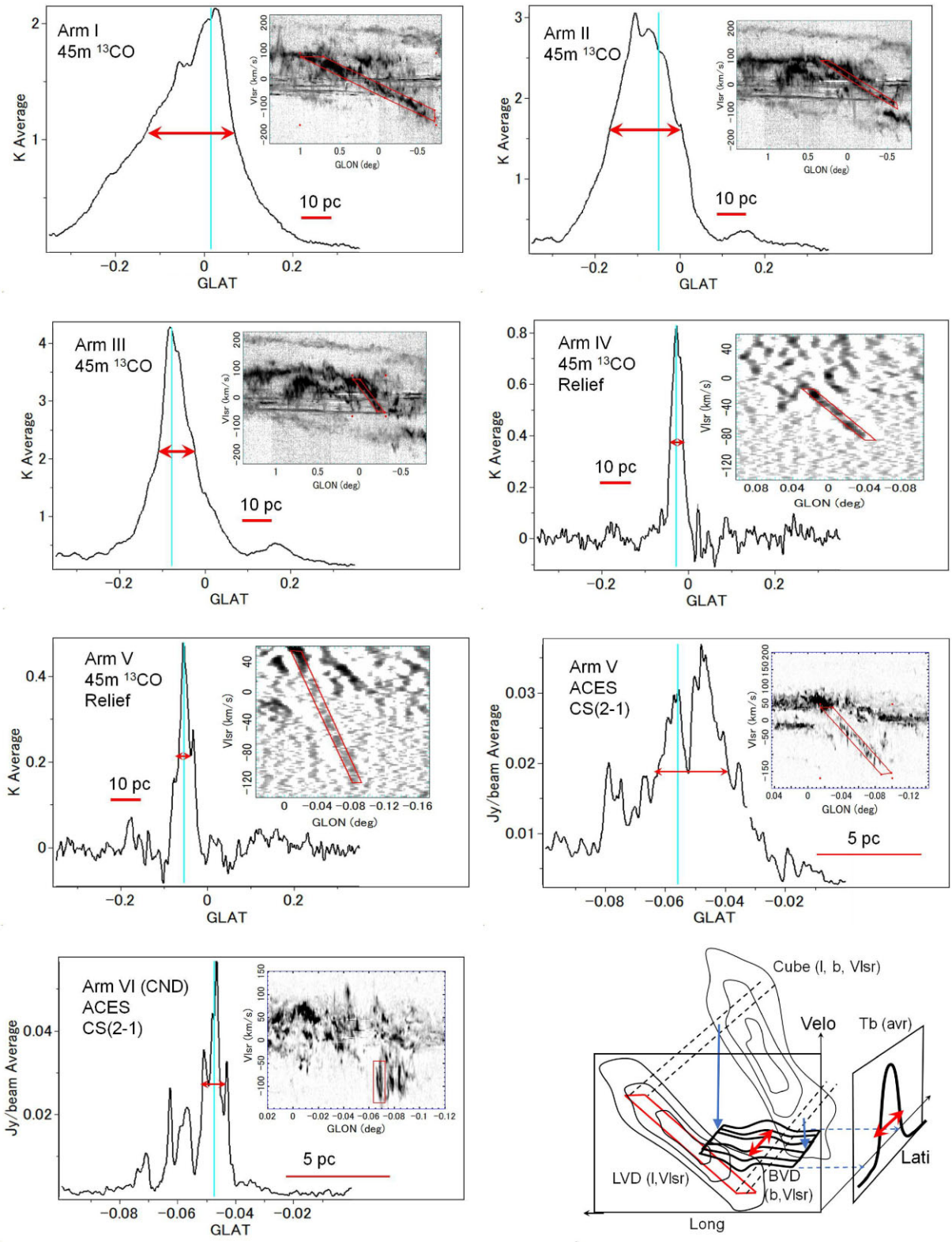


**Fig. 8.** Latitudinal profiles in the $^{13}$CO ($J = 1$–0) and CS ($J = 2$–1) line emissions of Arms I to VI averaged in the regions along the LV ridges as marked by the red boxes in the insets. The latitudinal full width at half maximum (FWHM), $z$, was measured as the red arrows. The bottom-right image explains the procedure to obtain the latitudinal profile using SAOimage (ds9).

**Table 1.** Parameters of the GC arms inferred from the $dv/dl$ method.[†]

| Arm | $dv/dl$ (km s$^{-1}$ deg$^{-1}$) | $\Delta l$ (°) | $v^*_{\rm LSR}$[‡] (km s$^{-1}$) | $R$[§] (pc) | $P$ (Myr) | $z_{\rm full}$ (pc) | $\hat{i}$ (°) | Arm volume ratio[‖] $\mathrm{Vol_N/Vol_{Arm\ I+II}}$ |
|---|---|---|---|---|---|---|---|---|
| Arm I | 150. | +0.25 | −40 | 141. | 5.9 | 26 | 4 | For I+II = 120 pc ring |
| Arm II | 212. | −0.1 | +10 | 101. | 4.2 | 20 | | =1.0 |
| Arm III | 507. | −0.1 | +50 | 42. | 1.7 | 4.7 | | $\sim 2\times10^{-2}$ |
| Arm IV | 1020. | +0.08 | −80 | 21. | 0.86 | 3.6 | | $\sim 3\times10^{-3}$ |
| Arm V | 2600. | +0.025 | −50 | 8.2 | 0.34 | 3.1 | 21 | $\sim 4\times10^{-4}$ |
| Arm VI (CND) | 9300. | 0 | 0 | 2.3[**] | 0.1 | 1.4 | 29 | $\sim 10^{-5}$ |
| Arm VII (mini-spirals)[♯] | $\sim 10^4$ | – | – | ∼1.2 | ∼0.05 | ∼1.4 | ∼36 | $\sim 10^{-5}$ |

[†]The inclination angle is assumed to be $i \simeq 90°$ (tilt angle $\hat{i} = 0°$), except for Arm VII.
[‡]$v^*_{\rm LSR}$ is $v_{\rm LSR}$ at $l = -0.^\circ056$ (Sgr A*). The reference center is taken at Sgr A* with $(l, b) = (359.^\circ944227, -0.^\circ046157)$.
[‡]$R \propto V_{\rm rot}R_0$: Here we assume $V_{\rm rot} = 150$ km s$^{-1}$ and $R_0 = 8.2$ kpc.
[‖]The ratio of the volume shared by Arm $N$ to that of the 120 pc ring composed of Arms I and II as calculated by $\mathrm{Vol_N} = \pi R^2 \times z$.
[♯]Approximate values read on the maps in the literature (Zhao et al. 2009; Tsuboi et al. 2017).
[**]Consistent with the current measurement $R \simeq 2.5$ pc (Tsuboi et al. 2018).
[††]Read from the LVD of Takekawa, Oka, and Tanaka (2017).

indicates that Arm II is tailing from Sgr C, extending nearly symmetrically to Arm I from Sgr B, and extends further to the west along the horizontal LVR Link I–II beyond the edge of Arm II. Panel (D) presents part of Arm II in the moment-0 map traced by the tilted straight LVR alone.

The molecular gas mass of the CMZ is shared mostly by these two main Arms I and II as discussed below in subsection 4.5. The two arms have been proposed to compose the main 120 pc ring (Sofue 1995) of the CMZ, and have been extensively studied in order to derive the 3D structure of the CMZ (Molinari et al. 2011; Kruijssen et al. 2015; Henshaw et al. 2016; Tokuyama et al. 2019; Sofue 2022). It is further suggested that the arms are related to the outer star-formation region Sgr E ($l \sim -1°$) and supernova remnants Sgr D ($\sim +1.^\circ2$), drawing a double infinity ($\infty\infty$) on the sky (Sofue 2022). However, the degenerate Arms I and II are resolved in the LV space, and the masked moment-0 map (figure 9) shows a simple tilted ring.

### 3.3 Arm III

Arm III has not been studied in detail so far in spite of its high brightness. It is visible in $^{13}$CO ($J$ = 1–0) in the LVD in figure 3 and in the moment-0 maps in figures 9 and 10. The LV ridge of this arm is composed of two parallel stripes in the H$^{13}$CN ($J$ = 1–0) and HCN ($J$ = 4–3) lines. The line spectrum shows a clear center-velocity absorption along this arm as shown by the inset in panel (E) of figure 9. The absorption belt along Arm III will be discussed in some detail later in subsection 5.3.

This arm seems to consist of the GMC M−0.13−0.08 (20 kmC) (see Takekawa et al. 2017). The moment-0 map in figure 3 shows a rather short arm on the sky, being led by a bright clump of 20 kmC. If 20 kmC is physically associated with Arm III, its 3D position can be determined kinematically, as will be done in subsection 4.1. Thereby, we assume that Arm III is in front of Sgr A*, following the face-on geometry proposed by Takekawa, Oka, and Tanaka (2017).

However, it has also been suggested that there is a physical contact between the +20 km s$^{-1}$ cloud and the CND (Takekawa et al. 2017). If this is the case, a different view is required, and Arm III may be redefined as a long bright ridge only in negative $v_{\rm LSR}$, extending to $(l, v_{\rm LSR}) \sim (-0.^\circ2, -50$ km s$^{-1})$. Another concern is its possible relationship with to 50 kmC: As shown in the relieved LVD in figure 3, 50 kmC is located on the increasing-longitude extension of Arm III. In this paper, we examine another possibility that 50 kmC is related to Arm V not only for the LV position but also for the large $dv/dl$ value close to that of Arm V and the large velocity width (subsection 5.3).

### 3.4 Arm IV

Arm IV is the arm most clearly visible in the relieved $^{13}$CO ($J$ = 1–0) LVD at negative $v_{\rm LSR}$ as shown in the bottom panel of figure 4. Its positive-$v_{\rm LSR}$ extension is visible in the original LVD as indicated in the middle panel of this figure, but is strongly disturbed by the contamination from Arms I and II as well as the extended CMZ emission.

This arm can be clearly traced on the LVD in figure 4, and is also visible on the moment-0 map in CS ($J$ = 2–1) from ACES. The arm runs westward from $l \sim 0.^\circ02$ and ends at $l \sim -0.^\circ04$.

Part of this arm has been identified as the "C1" clump at $(l, b, v_{\rm LSR}) \simeq (-0.^\circ03, -0.^\circ06, -70$ km s$^{-1})$, which shows intense CS emission (Oka et al. 2011).

### 3.5 Arm V

Arm V is a long, straight LV ridge composed of a low-brightness stripe extending from $(l, v_{\rm LSR}) = (-0.^\circ02, +30$ km s$^{-1})$ to $(-0.^\circ1, -130$ km s$^{-1})$, as shown in figure 5. In the moment-0 map in CS ($J$ = 2–1) (figure 10C), Arm V runs at position angle PA $\sim 25°$, and is approximately fitted by an ellipse of axial ratio $b/a \sim 0.25$ or an inclination angle of $i \sim 76°$ (tilt angle $\hat{i} \sim 14°$). 50 kmC is located on the positive-velocity extension of Arm V in the LVD, and the velocity gradient is about equal to that of Arm V (see subsection 5.3).

### 3.6 Arm VI: CND

The CND (Wright et al. 2001; Montero-Castaño et al. 2009; Martín et al. 2012; Feldmeier et al. 2014; Mills et al. 2017; Tsuboi et al. 2018; Hsieh et al. 2021) is recognized in the CS ($J$ = 2–1) and H$^{13}$CN ($J$ = 1–0) lines in the LVDs in figure 6 as a bright highly tilted ridge extending from $(-0.^\circ04, +120$ km s$^{-1})$ to $(-0.^\circ07, -130$ km s$^{-1})$ indicating a rotating ring. We call this ring Arm VI, which is equivalent to CND.

We stress that the arm is barely visible in the $^{13}$CO ($J$ = 1–0) line, becoming clearer in the LVDs of CS ($J$ = 2–1), H$^{13}$CN ($J$ = 1–0), and HCN ($J$ = 4–3). This demonstrates that the

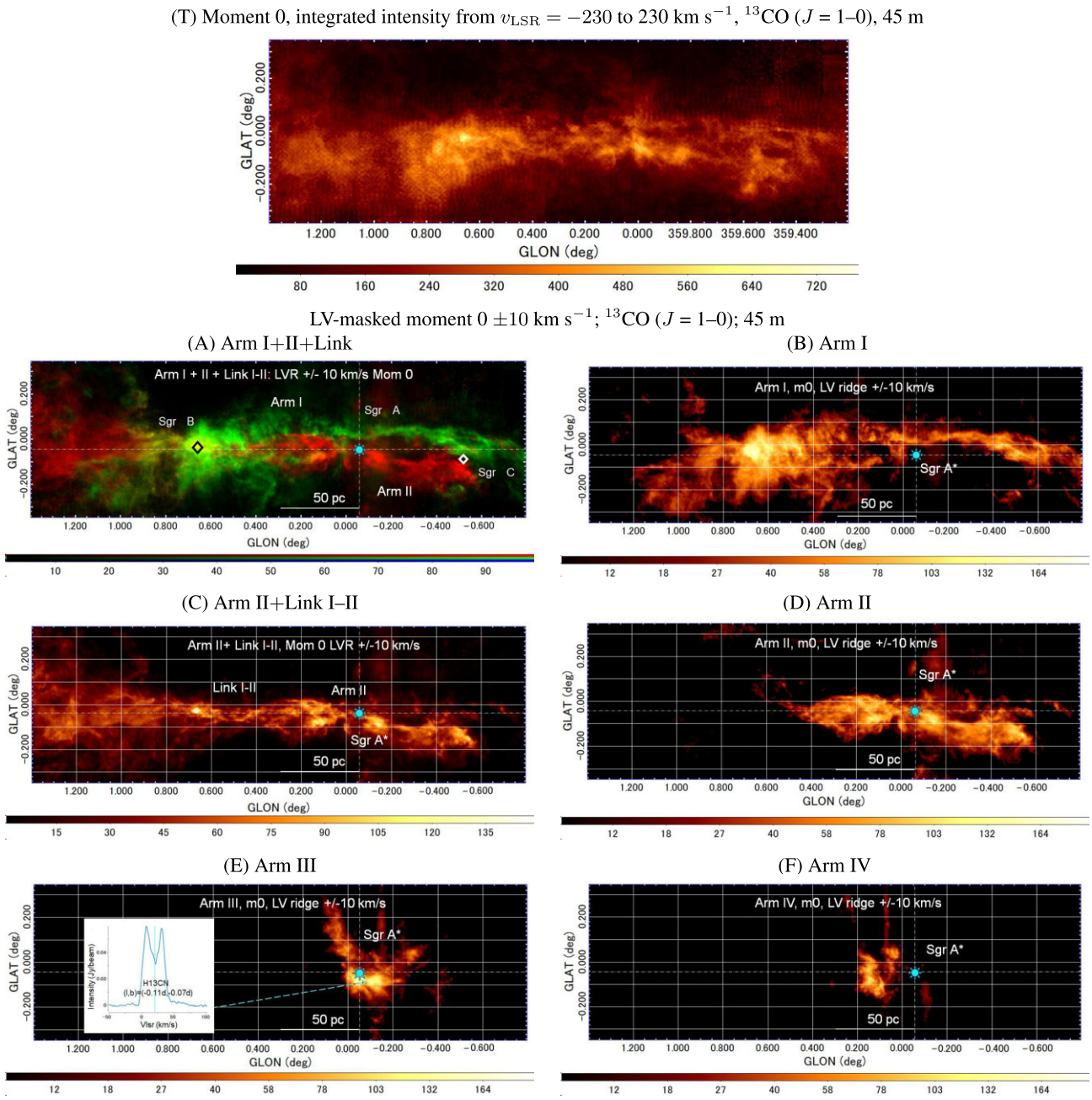


**Fig. 9.** Integrated intensity (moment-0, [K km s$^{-1}$]) maps in $^{13}$CO ($J$ = 1–0) of the GC arms from Nobeyama 45 m at a resolution of 16.″7. (T) Whole-area total integrated intensity (moment-0) map in the $^{12}$CO line by the 45 m telescope. (A) Arm I (green) + II + Link I–II (red) integrated intensity within ±10 km s$^{-1}$ from the LV ridge (same below); (B) Arm I; (C) Arm II + Link I–II along the bent LVR in figure 2; (D) Arm II (straight LVR alone); (E) Arm III; and (F) Arm IV. The color bars indicate the integrated intensity (moment 0) in K km s$^{-1}$. A H$^{13}$CN ($J$ = 1–0) line spectrum of Arm III at ($l$, $b$) = (−0.°11, −0.°07) is inset in panel (E).

molecular gas in the CND (Arm VI) is much denser and warmer than the general CMZ clouds such as in Arms I and II. The LV ridge exhibits a double-peaked rotating ring structure whose central part is missing. A curved spur extends from the negative-velocity end of Arm VI, indicating that the arm is associated with a high-velocity non-circular flow.

Figure 11 shows the moment-0 maps of Arm VI in CS ($J$ = 2–1) and H$^{13}$CN ($J$ = 1–0) as integrated within $\delta v_{\rm LSR} = \pm 7$ and ±10 km s$^{-1}$ from the LV ridge (LVR), respectively, which agree with the CS ($J$ = 7–6) map using ALMA by Tsuboi et al. (2018). The figure exhibits an elongated ellipse centered on Sgr A* as marked by the dashed line in the bottom panel of figure 11, which has an axial ratio of $b/a \sim 0.^{\circ}0085/0.^{\circ}023 = 0.405$ at a position angle of the major axis of PA $\sim 70^{\circ}$. If it is a circular ring, the inclination angle is $i \simeq 66^{\circ}$ (tilt angle $\hat{i} \sim 24^{\circ}$). Several spiral arms and fins are bifurcating from the ring, trailing in the sense of counterclockwise rotation in the figure (on the sky).

The positive-latitude side of the ring (northern wing) is missing (figure 11, bottom panel), although it is visible in the warm $H_2$ (2.4 μm) emission (Feldmeier et al. 2014; Mills et al. 2017). The difference in the characteristics in the mm and μm emissions may be attributed to absorption of Sgr A's continuum emission by the CS and H$^{13}$CN molecules.

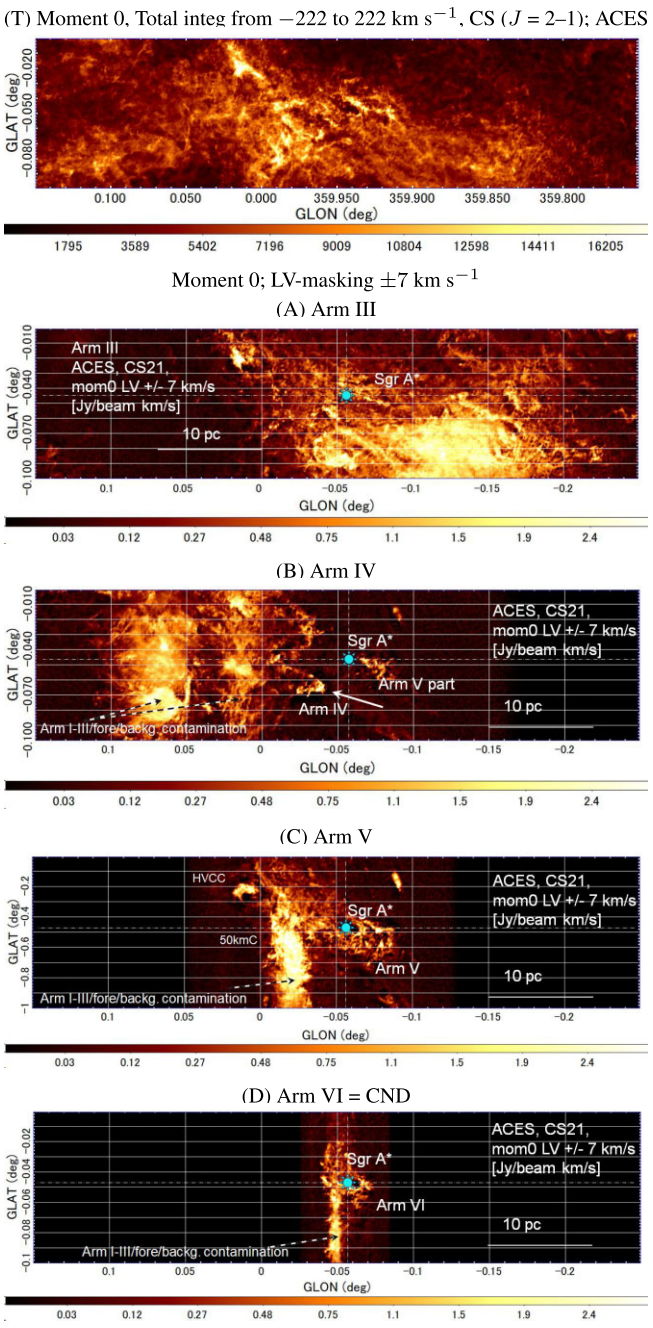


**Fig. 10.** (T) ACES CS ($J$ = 2–1) integrated intensity (moment 0; [Jy beam$^{-1}$km s$^{-1}$]) over the entire velocity range from −220 to 220 km s$^{-1}$, and (A)–(D) along LV ridges with $v_{\rm LSR}$ within $\delta v = \pm 7.5$ km s$^{-1}$ for Arms III to VI (CND) at a resolution of 2.″2. Vertical broad bands are contamination of the extended emission of CMZ and Arms I and II. Color bars indicate the integrated intensity (moment 0) in Jy beam$^{-1}$ km s$^{-1}$.

In contrast, the negative-latitude side (southern wing) draws a nearly perfect ellipse, indicating no absorption. These suggest that the northern wing of the ring is in front of Sgr A and the southern half is beyond it. This is consistent with the counter-clockwise rotation of the disk seen from below the Galactic plane. There is a hole in the center of the ring coinciding with Sgr A*, which is due to the absence of molecular gas around the mini-spirals at high temperature and due to absorption of Sgr A's continuum emission.

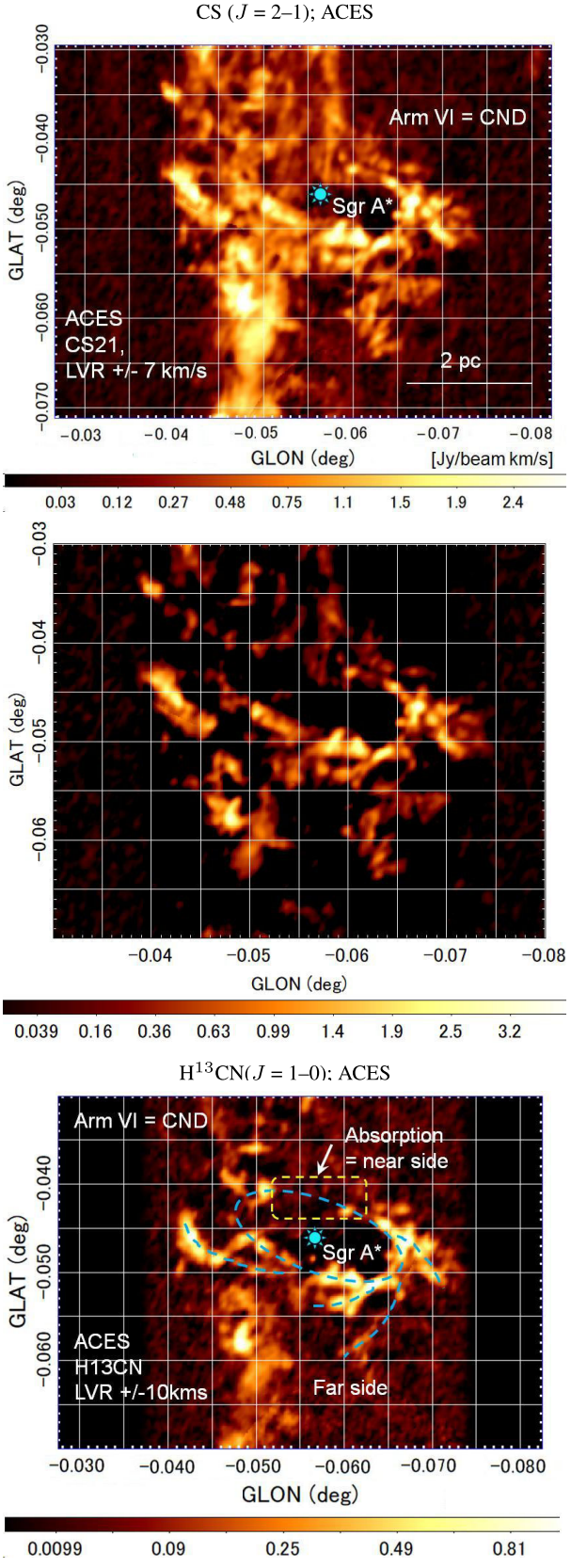


**Fig. 11.** [Top] Arm VI (CND) in CS ($J$ = 2–1), same as figure 10, but close up. [Middle] Same, but the vertically extended components due to fore-/background emission have been removed. [Bottom] Same, but in H$^{13}$CN ($J$ = 1–0). An ellipse is seen associated with spiral fins, indicating a ring with inclination angle $i \sim 65°$.

### 3.7 Arm VII: Mini-spirals

The mini-spirals are composed of ionized gas (Tsuboi et al. 2017) and are not detected in the present data. They rotate around Sgr A* in elliptical orbits of radius ∼1.2 pc and inclination $i \sim 126^\circ$ ($\hat{i} \sim 36^\circ$) (Zhao et al. 2009), and therefore have a vertical extent $z \sim 1.4$ pc. Interestingly, they are on a natural extension of the radius–vertical extent and radius–inclination relationships among the arms as discussed in subsection 4.2. Although they are outside our direct analysis based on the molecular-line observations, we suggest that the minispirals be the innermost family of the GC Arms, and call them Arm VII.

### 3.8 Fine LV stripes

Besides the large-scale, grandly designed arm structures that trace the tilted LV ridges spanning ∼±100 km s$^{-1}$ like Arms I to VI, there are numerous fine stripes composed of shorter (∼±10–30 km s$^{-1}$) vertical LV ridges seen in the relieved LVDs from the 45 m telescope (appendix 1, figure 18) and in the ACES LVDs at higher resolution with ∼ ± 10 km s$^{-1}$ (figure 7). They are mostly individual molecular clouds that are not resolved in the longitude direction, indicating that the CMZ contains numerous clouds with sizes smaller than the beam width ∼2″ ∼ 0.1 pc and velocity dispersions of ∼10–30 km s$^{-1}$.

We point out that some such LV ridges (individual clouds) are inclined in the same sense as that caused by the Galactic rotation, but generally with tilt angles steeper than those of the main Arms I and II. This suggests that some of the LV ridges, except for the innermost LV ridges discussed in the next section, represent individual clouds locally rotating more rapidly than the disk's rotation due to self-contraction with the cloud's angular momentum being conserved.

## 4 Arm radius and vertical extent

### 4.1 Radii of GC arms using the $dv/dl$ method

Here we introduce three observable quantities to describe the identified arms on the LVD: (1) velocity gradient (slope) $dv/dl$ of the LV ridge, (2) velocity intersection $v^*_{\rm LSR}$ of the ridge at the longitude of Sgr A* at $l = -0.^\circ056$, and (3) peri-/apocentric longitude offset $\Delta l_0$ from Sgr A*, at which the motion of gas becomes perpendicular to the line of sight so that $v_{\rm LSR} = 0$ km s$^{-1}$. Table 1 lists the values of $dv_{\rm LSR}/dl$, $v^*_{\rm LSR}$, and $\Delta l$ measured by eye-fitting to the corresponding LV ridges in the LV plane.

If we assume that an extended object is rotating around a certain center in an edge-on disk, the curvature of the flow line, $R$, is related to the velocity gradient by

$$R \simeq R_0 V_{\rm rot} \left( \frac{dv_{\rm LSR}}{dl} \right)^{-1}, \tag{3}$$

where $V_{\rm rot} \sim 150$ km s$^{-1}$ is the rotation velocity. If we assume that the flow is circular around Sgr A*, the radius is equal to the galactocentric distance $R$.

The error in the curvature propagates from that in the measurement of $dv/dl$, which is about ±5%, and the uncertainty of the rotation velocity, which causes an error of a factor of 1.5 (100–150 km s$^{-1}$). Therefore, the error in the curvatures/radii of the arms determined in this paper is a factor of ∼1.5 mostly attributed to the accuracy of the assumed rotation velocity.

Note that this method measures the local curvature of the streamlines for a given flow velocity. Even if the flow is not circular, e.g., elliptical, hyperbolic, etc., it gives the local streamline curvature. It works even if the flow is overlapped by radial expansion or contraction, because $dv_{\rm expa}/dl \simeq {\rm O}(\theta^2) \simeq 0$ near the rotation axis with $v_{\rm expa}$ and $\theta$ being the expanding/contracting velocity of the disk (arm) and galactocentric longitude, respectively. This method measures the curvature of the streamline, but not the curvature of the density distribution such as a filament or arm that may be inclined at an angle to the streamline in such a case of Galactic shock waves.

In the case of Arm IV, for example, we measure the velocity gradient to be $dv_{\rm LSR}/dl \simeq 200$ km s$^{-1}$ per $0.^\circ02$ in the LVDs, resulting in $R \simeq 21$ pc, assuming $i \sim 90^\circ$ and $j \sim 0^\circ$. The rotation period is then $P = 2\pi R/V_{\rm rot} \sim 0.86$ Myr.

Table 1 lists the estimated values of $R$ and $P$ for the identified arms obtained for $R_0 = 8.2$ kpc and $V_{\rm rot} = 150$ km s$^{-1}$. In the top panel of figure 12 we show the "arm–radius relation," or a plot of radii against arm number I to VII, where Arm VII represents the mini-spirals as discussed later. The plot is approximately fitted by

$$R \sim R_{\rm A} \left( \frac{V_{\rm rot}}{150 \text{ km s}^{-1}} \right) \times (2/5)^N \text{ pc}, \tag{4}$$

($N$ = I, II,..., VII) within an error of factor ∼2, where $R_{\rm A} = 630$ pc. This shows that the existence of the arms is discrete and that the ratio between the radii of two neighboring arms/rings is ∼2.5, suggesting a Bode's law-like arm structure. Alternatively, it may be attributed to a logarithmic spiral with a pitch angle of $p \sim 22^\circ$.

### 4.2 Face-on view of GC arms

Using the estimated radii of the arms, their orientations in the CMZ are illustrated in figure 13. The top panel shows a schematic sketch of the CMZ projected on the sky, a cross-section of the warping arms, and an oblique view of the resolved arms and rings.

The second panel shows face-on views of the arms using their calculated radii from the $dv/dl$ method, where the thick lines show a face-on view of the arms with determined radii. The longitudinal offsets of the nodes at $v_{\rm LSR} = 0$ km s$^{-1}$ are marked by red lines, and dashed red lines represent position angles $\theta$ of Sgr B and C with respect to the curvature center. Dashed gray lines illustrate suggested connections to the outer disk (Sawada et al. 2004). Position angles of the associated molecular clouds with respect to Sgr A* are calculated by $\theta = \sin^{-1} v_{\rm LSR}/V_{\rm rot}$ ($v_{\rm LSR} = 150$ km s$^{-1}$).

The bottom panel shows the inner arms, where the thick curves represent the measured radii with the curvature centers shifted to the $v_{\rm LSR} = 0$ km s$^{-1}$ nodes. Gray ellipses illustrate possible orbits of the arms that satisfy the derived radii. The result is globally consistent with the face-on views obtained using the intensity ratio of the CO line emission to the OH absorption line (Sawada et al. 2004; Yan et al. 2017).

We have so far assumed that the orbits of the arms are circular around a center at the longitude at which the LV ridge crosses the $v_{\rm LSR} = 0$ km s$^{-1}$ line. Although this assumption leads to a reasonable galactocentric distance $R$ using the $dv/dl$ method, to map the arms and clouds more precisely, we need a realistic gravitational potential and a flow line model around

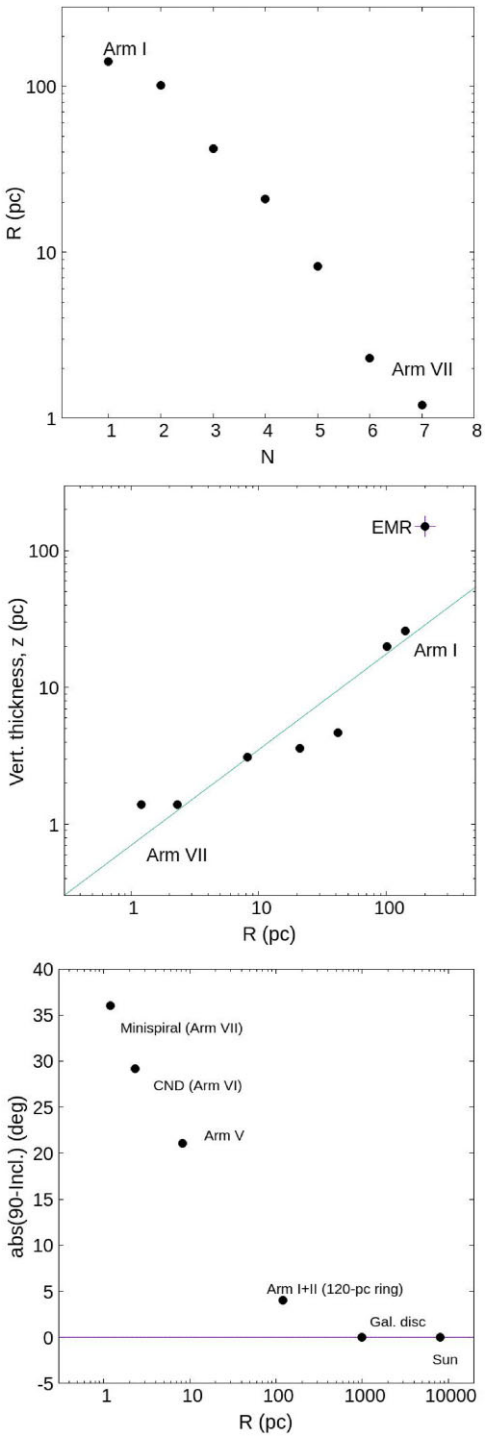


**Fig. 12.** [Top] Arm radius-to-number relation, which is expressed by $R \sim 630 \times (2/5)^N$ pc with an error of factor ~2. [Middle] Vertical extent, $z$, of Arm VI to Arm VII (mini-spirals) plotted against radius $R$. The straight line represents $z = 0.7(R/1\ \mathrm{pc})^{0.7}$ pc. The big cross indicates EMR. [Bottom] Absolute values of the 90° inclination angle of the arms/rings plotted against radius.

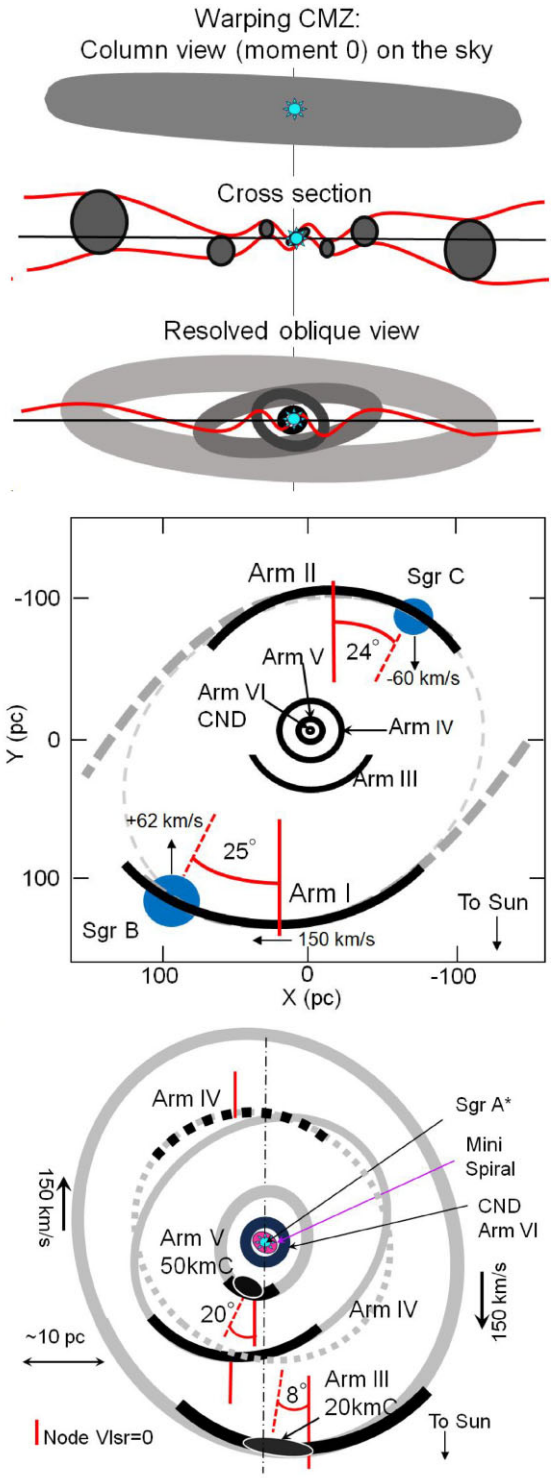


**Fig. 13.** [Top] Schematic view of the CMZ projected on the sky, a cross-section of the warping arms, and an oblique view of the resolved arms/rings. [Middle] Proposed face-on distribution of the GC arms. Thick lines show the arms with determined radii. Vertical red bars indicate the nodes of $v^*_{\mathrm{LSR}} = 0$ km s$^{-1}$, and dashed red lines show the position angles $\theta$ of Sgr B and C with respect to the curvature center. Dashed gray lines illustrate suggested connections to the outer disk (Sawada et al. 2004). [Bottom] Same, but for arms further in. The thick curves represent the radii measured with the center of curvature shifted to the node of $v_{\mathrm{LSR}} = 0$ km s$^{-1}$. The gray ellipses show the possible orbits of the arms that satisfy the derived radii. Arms III and V are on the near side of Sgr A due to absorption of the continuum emission of Sgr A. A near/far answer for Arm IV is not given in this study.

Sgr A (e.g., Kruijssen et al. 2015, 2019), which is, however, beyond the scope of this paper.

### 4.3 Vertical extent decreasing toward the nucleus

In subsection 2.5 we have shown that the vertical extent of the arms increases with the radius $R$. In figure 12 (middle panel)

we plot the full extent $z$ of the arms against the arm radius $R$. Here, we also plot the supposed vertical extent of the mini-spiral (Arm VII) of ∼1 pc from the literature. In this log–log plot, the extent is approximately expressed by a straight line given by

$$z \sim 0.7(R/1\ \mathrm{pc})^{0.7}\ \mathrm{pc}. \quad (5)$$

Since the measured vertical extents of the arms may be considered to represent upper limits to the thickness of the disk, this plot indicates that the thickness of the CMZ disk decreases toward the nucleus. This means that the disk inside Arms I and II becomes thinner from a few pc to ∼1 pc near Sgr A.

However, note that these latitude profiles do not include clouds such as the Sgr B complex in Arm I and 50 kmC in Arm V, which extend more vertically than expected from the $R$–$z$ relation. This raises the question of whether these clouds are physically associated with the arms and how such vertical protrusions could have formed from the thin arms. Alternatively, such "high-$z$" clouds may manifest large bends (oscillations) in the trajectories or more deviated inclinations of orbits from $i \sim 90^\circ$.

We also point out that the vertical extent of the 200 pc expanding molecular ring (EMR) ($z \sim 150$ pc) at radius ∼200 pc (Sofue 2017) deviates significantly from the fit to the arms, as shown by a large cross in figure 12. This will be touched upon in subsection 5.4.

### 4.4 Tilt angle of disk increasing toward nucleus: Warping CMZ

As shown in the moment-0 maps (figures 9 and 10), the 120 pc ring consisting of Arms I + II, Arm V, and Arm VI (CND) exhibits elliptical structures on the sky, indicating that the rings deviate significantly from the edge-on orientation. Arm III does not appear as a clear ellipse, but its ridge is tilted a few degrees from the horizontal, which may represent a tilt of the ring. Arm IV is too divergent in the moment-0 map to define a corresponding ellipse. The mini-spiral (Arm VII) is well known for its highly tilted orientation with a minor to major axis ratio of $b/a \sim 0.5$.

We then calculate the "tilt angle" $\hat{i} = 90^\circ - i$ of the ring's rotation axis from the Galaxy's rotation axis. The inclination is measured using the ratio of the minor and major axes of an ellipse as well as the tilt angle of the major axis of the arms (ellipses) on the sky in the moment-0 maps. Plotting the results in the last panel of figure 12, we see that the tilt angle increases rapidly with decreasing radius toward the nucleus.

This behavior can be explained in terms of the gas accretion caused by the Galactic shock wave as follows: The angular momentum $A_z$ of the gas about the rotation axis is effectively transferred by the oval motion in the barred potential, while the perpendicular component of the angular momentum $A_x$ is conserved. This causes a faster loss of $A_z$ than $A_x$ until the radius becomes comparable to the $z$ extent, when $A_z$ becomes comparable to $A_x$, as observed in the central region with Arms V to VII. The magnetic twist mechanism (Shibata & Uchida 1986) may work similarly, acting to transfer the angular momentum of a rotating gas disk penetrated by strong vertical magnetic field (Heywood et al. 2022).

### 4.5 Relationship of the arms to the general CMZ structure

We next estimate the relative luminosity (∼mass) of the GC arms to that of Arms I + II, or the 120 pc ring, using the arm radii $R$ in table 1 and their vertical extent $z$. Assuming about the same molecular line brightness (within an order of magnitude), the relative luminosity of Arm $N$ to that of Arms I + II is estimated by

$$L_N/L_{\mathrm{I+II}} \sim (R_N/R_{\mathrm{I+II}})(z_N/z_{\mathrm{I+II}}), \quad (6)$$

where $N$ stands for arm number I to VII and the subscript I+II stands for average of the quantities of Arms I and II. We obtain the ratios to be $L_i/L_{\mathrm{I}} \sim 1$ (for Arms I, II); $\sim 2 \times 10^{-2}$ (III); $\sim 3 \times 10^{-3}$ (IV); $\sim 4 \times 10^{-4}$ (V); and $\sim 1.4 \times 10^{-5}$ (VI).

Arms I and II share most of the mass of the CMZ, composing the 120 pc molecular ring (or the "great ring"). Inside the ring the disk shares only a small portion of the CMZ's volume due to the decrease both in radius and vertical extent, or Arms III to VI share portions of the entire volume that are smaller by two orders of magnitude; hence the mass. This is consistent with the low infrared extinction in the nuclear stellar disk (Nogueras-Lara 2022).

The small volume (mass) of the disk inside Arms I and II means that the inflow from the CMZ ring into the nucleus is extremely slow; in other words, the ring is large enough to supply the inner arms, albeit with very low efficiency.

## 5 Discussion

### 5.1 General remarks

Henshaw et al. (2023) published a comprehensive review of recent progress in the study of the 3D molecular gas distribution of the CMZ in the $(l, b, v_{\mathrm{LSR}})$ space (see the literature therein). There seems to be a consensus that Arms I and II constitute the main structure of the CMZ, composing a large ring-like structure (the 120 pc ring) of radius ∼100–120 pc rotating clockwise around Sgr A* as seen from the North Galactic Pole. However, apart from some mentions of the existence of Arms III and IV, there has been no detailed study of the spiral arm or ring structure inside the 120 pc ring. In this paper, we show that there are many more inner arms including Arms III and IV of radii $R \sim 40$ and $\sim 20$ pc, respectively, and Arm V of radius ∼8.2 pc, which is identified here for the first time. The innermost structures such as the CND and mini-spirals can be understood as systems organized with a unified rule as Arms VI and VII, respectively.

The thus-identified arms are summarized in figure 13 and table 1. Since the present analysis focuses on the kinematical and geometrical structure of the CMZ, we have not calculated the density and mass. Therefore, the derived arms/rings appear rather symmetric to Sgr A*. The highly asymmetric distribution of the mass both in space and velocity known since the 1980s (Bally et al. 1987, 1988) is somehow suppressed in the present analysis. Converting the $T_{\mathrm{B}}(l, b, v_{\mathrm{LSR}})$ cube to a $\rho(x, y, z)$ cube for more quantitative modeling of the CMZ would be a subject for the future.

Theories and simulations to understand the distribution and motion of molecular gas in the GC have been extensively developed over decades, predicting different types of flow

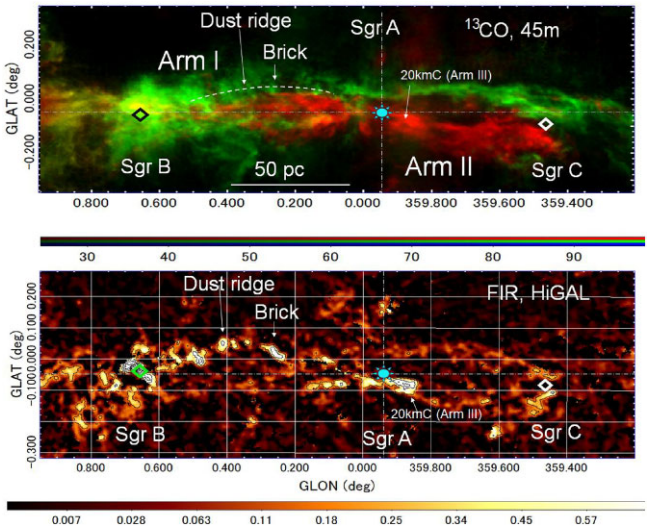


**Fig. 14.** [Top] Masked moment-0 map in $^{13}$CO ($J = 1$–0) Arms I (green) and II (red) (same as the top panel of figure 9) compared with [bottom] a Herschel FIR-derived dust column density map (Guzmán et al. 2015) with the intensity indicated by the bar in units of [grams cm$^{-2}$] and contours every 0.7 starting at 0.2. Note that 20 kmC at ∼G−0.0.025−0.07, which is located on the near side of Sgr A, is contaminated in the moment-0 map of Arm II (far side) in the top panel.

models in the CMZ and circumnuclear regions (Rodriguez-Fernandez & Combes 2008; Wada et al. 2011; Kim & Stone 2012; Krumholz & Kruijssen 2015; Krumholz et al. 2017; Ridley et al. 2017; Sormani et al. 2019, 2020; Tress et al. 2020): The simulations suggest that symmetric spirals of grand design mimicking Arms I and II are generated as a result of Galactic shock waves in a bar potential, carrying the gas to the innermost regions and giving rise to CND and mini-spiral-like structures. However, even if such a mechanism works, the efficiency of the inward flow must be extremely low, because the mass ratio between the innermost arms and the entire CMZ is very low, as shown in table 1. The proposed new view of the innermost spiral structure, including the CND and mini-spirals (associated with Arms VI and VII, respectively), would provide further observational constraints on the model and add information to a more precise understanding of the CMZ.

Below we discuss some specific topics related to the individual arm structures.

## 5.2 Comparison with the far-infrared dust map

### 5.2.1 Arms I and II in dust emission

We show in figure 14a preliminary comparison of the arm structure in the $^{13}$CO ($J = 1$–0) line with the image of the CMZ in a dust column density map computed from the Herschel HiGAL survey at 70, 160, 250, 350, and 500 μm. The data set was reprocessed with an algorithm designed to obtain more accurate measurements of cold, dense filamentary structures, densities, and temperatures, by improved subtraction of diffuse foreground and background emission. The five Herschel bands were convolved to the resolution of the 500 μm SPIRE image and a process based on the CUPID-findback algorithm was repeatedly applied until consecutive iterations differed by less than 5% in all pixels (see also Etxaluze et al. 2011). Taking an estimated value for the dust beta of 1.6, we derived a dust temperature map that, combined with the flux map, yielded a dust column density map. Additional details about the method and reliability checks are given in Guzmán et al. (2015).

It is clear that the warped dust ring coincides closely with the molecular-line ring composed of Arms I and II, where Arms I and II are located on the near and far sides of Sgr A*, associated with Sgr B and C, respectively. However, note that Arm II near Sgr A in this moment-0 map is contaminated by Arm III associated with 20 kmC. The infinity shape suggested in the earliar integrated-intensity maps in molecular lines and dust emission (Molinari et al. 2011) can be traced in the far-infrared (FIR) dust map, whereas it does not show up so clearly here in the $^{13}$CO ($J = 1$–0) map resolved in the $(l, b, v_{\rm LSR})$ space. Interestingly the dust "Brick" (G+0.25+0.02) (Henshaw et al. 2019; Walker et al. 2021; Ginsburg et al. 2023) is clearly seen in the FIR, but is hardly visible in this CO map, which indicates that the cloud is displaced from the molecular arms, or the LV-masking function used here was too simple. Arm III, which is not shown here in $^{13}$CO ($J = 1$–0), is visible in the FIR map as a short horizontal belt near Sgr A*.

### 5.2.2 The Dust Ridge and the Brick

The positive-longitude side of Arm I in the CO line is well correlated with the Dust Ridge composed of a chain of the massive dark cloud Brick G+0.0253+0.016 and Clouds b, c, d, e/f in the far-infrared emission and absorption (Henshaw et al. 2019; Ginsburg et al. 2023; Sofue 2024; Lu et al. 2024; Battersby et al. 2025), showing a good coincidence with each other. However, the Brick in CO in this map shows up only partially, because the radial velocity is about 20 km s$^{-1}$ displaced from the main ridge of Arm I, as shown in figure 1, so that the CO line moment-0 map misses the major part of the cloud. The Brick exhibits an oppositely tilted LV ridge (figure 1) superposed by an expanding-shell structure, which may be attributed to a peculiar shear motion of the cloud (Petkova et al. 2023).

### 5.2.3 Far-infrared clouds "Stone, Straw, and Sticks"

The molecular clouds called "Stone, Straw, and Sticks" draw a horizontal belt around $(l, b) \sim (+0.^{\circ}08, -0.^{\circ}08)$ (Battersby et al. 2020), and appear in the moment-0 map of Arm II in figure 9(D). They appear as an LV ridge in figures 2, 3, and 7 (top panel), running from $(l, v_{\rm LSR}) = (0.^{\circ}05, 50$ km s$^{-1})$ to $(0.^{\circ}15, 60$ km s$^{-1})$. Coincidence in the LV plane indicates that the clouds are associated with Arm II, and are not linked to 50 kmC, although apparently close on the sky. We point out that the 8 μm image of the GC (Stolovy et al. 2006) reveals almost no absorption toward these clouds, indicating that they are in the far side of the GC stellar bulge. However, the Brick and the Dust Ridge exhibit heavy extinction of the bulge stars, locating them in the near side. These locations of the clouds are consistent with those of Arms I (near) and II (far).

## 5.3 20 and 50 km s$^{-1}$ clouds

The inner region $|l| \lesssim 0.^{\circ}2$ (∼30 pc) around Sgr A* contains two well known molecular clouds: 20 kmC and 50 kmC (Herrnstein & Ho 2005; Tsuboi et al. 2009; Takekawa et al. 2017; Uehara et al. 2019). We comment on these clouds, which are visible and resolved in our data.

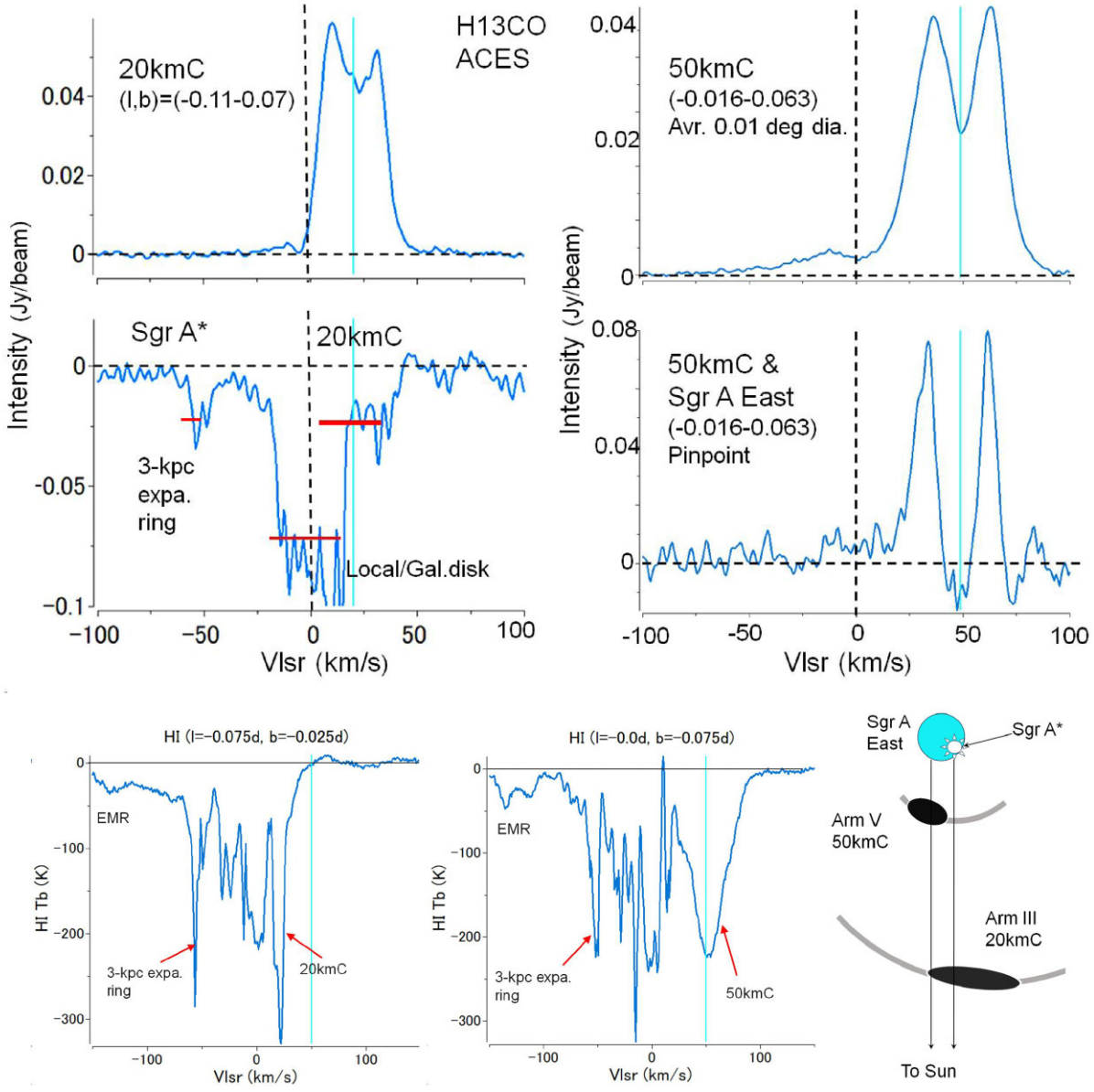


**Fig. 15.** [Top left] $H^{13}CN$ ($J = 1$–0) line profile of 20 kmC at ($l$, $b$) = (−0.°11, −0.°07) by ACES, showing self-absorption. The bottom panel shows the profile toward Sgr A*, showing absorption of the continuum emission by 20 kmC as well as local and disk clouds on the near side of the nucleus. [Top right] $H^{13}CN$ ($J = 1$–0) line profile of 50 kmC at (−0.°016, −0.°063) averaged in 0.°01 diameter, showing self-absorption plus absorption of the background continuum emission. Note the line width, which is twice as large as that of 20 kmC. The bottom panel shows a pinpoint profile at the same position toward the radio-bright edge of Sgr A East. The negative-intensity absorption of the continuum emission of Sgr A East puts 50 kmC in the near side. [Bottom left] H I line absorption toward 20 kmC at G−0.075−0.025 averaged in a circular field of diameter 0.°05 taken from the ATCA H I survey of the GC (McClure-Griffiths et al. 2012). Note the sharp absorption line of 20 kmC. [Bottom middle] Same, but 50 kmC at G+0.0, −0.075. Note the broad absorption line of 50 kmC. [Bottom right] Schematic illustration of the near–far solutions for 20 kmC and 50 kmC using absorption of the radio continuum emission.

### 5.3.1 Line-of-sight locations of 20 kmC and 50 kmC

We first consider the line-of-sight locations of the two clouds using absorption profiles of the molecular line spectra shown in figure 15. 20 kmC shows a clear double-horn profile indicative of self-absorption. The pinpoint spectrum on Sgr A* exhibits negative intensity absorption, indicating that the continuum emission is absorbed by 20 kmC, so that the cloud is on the near side of Sgr A*. 50 kmC also shows double horns toward the edge of Sgr A East, and a pinpoint spectrum exhibits negative intensity absorption. This indicates that the cloud is on the near side of Sgr A East, consistent with the earlier result (Tsuboi et al. 2009).

We applied the same method to the H I line using the Australia Telescope Compact Array (ATCA) survey of the GC (McClure-Griffiths et al. 2012). The bottom panels of figure 15 show the H I line spectra toward 20 kmC. Both spectra show deep absorption lines. Note also that 50 kmC has a much wider line width.

We have thus proved that radio continuum emission from Sgr A is absorbed by 20 kmC and 50 kmC in the molecular and H I lines, and we conclude that the two clouds are on the near side of Sgr A*. This is consistent with the near-side location of the two clouds inferred from the dust extinction analyses by infrared observa-

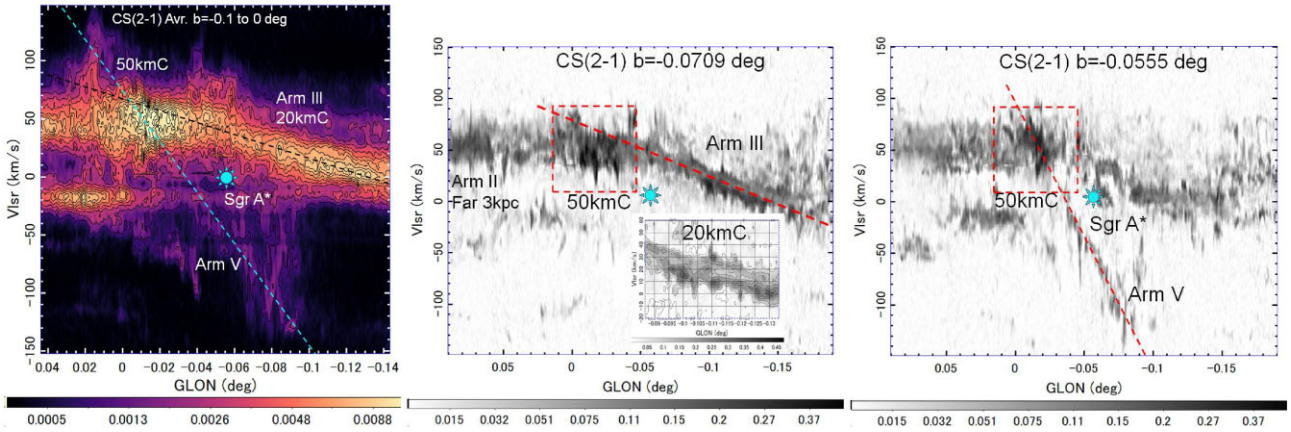


**Fig. 16.** [Top] Averaged LVD from $b = -0.^{\circ}1$ to $0^{\circ}$ in CS ($J = 2$–1) around 20 kmC and 50 kmC. Intensity scale is in Jy beam$^{-1}$ and contours are every1 mJy beam$^{-1}$ 1 mJy beam$^{-1}$. Dashed lines traces Arms III and V. [Middle] LVD at $b = -0.^{\circ}0709$ across 20 kmC and 50 kmC. Note the self-absorption belt along Arm III. 50 kmC is enclosed by the dashed box, and is enlarged in figure 17. [Bottom] LVD at $b = -0.^{\circ}055$ showing 50 kmC exactly on the extension of Arm V. Arm V is clearly visible in this diagram. 50 kmC is enlarged in figure 17. Note that Arm II and the 3 kpc expanding ring also intersect 50 kmC.

tions (Nogueras-Lara et al. 2021; Lipman et al. 2025; Walker et al. 2025).

### 5.3.2 20 kmC

In the top panel of figure 16 we show the LVD around 20 kmC and 50 kmC averaged in the full latitude range in the present analysis from $0^{\circ}$ to $-0.^{\circ}1$. The middle panel shows an LVD at $-0.^{\circ}071$ across the centers of 20 kmC and 50 kmC and along Arm III. The bottom panel is an LVD at $b = -0.^{\circ}055$ including Arm V.

20 kmC is aligned along the straight ridge of Arm III, which constitutes the main structure of the arm. There is no clear-cut boundary on either side of the cloud along the LV ridge, and the arm continuously extends toward both sides. This indicates that 20 kmC is not an isolated cloud.

The LV ridge of Arm III is separated by an absorption belt, which is a 2D view of the double-horn spectra. The double-horn absorption may be attributed to (i) an expanding cylinder (not a shell), (ii) absorption of the background continuum emission, or (iii) self-absorption. The possibility of an expanding cylinder (i) is unlikely considering the formation mechanism. We may also rule out an expanding spherical shell, which postulates an LV ellipse rather than an absorption belt. Absorption of background light (ii) is also unlikely because the region is ∼7 pc away from Sgr A on the sky, where the radio brightness is too low to cause absorption in the molecular line. We may therefore conclude that the feature is due to (iii) self-absorption along the arm.

We may thus conclude that 20 kmC is the densest part of Arm III with its 3D center position at $(x^*, y^*, z^*) \sim (-7.7, 42, -3.6)$ (pc). Here, $(x^*, y^*, z^*)$ are the Cartesian coordinates with respect to Sgr A* with the three axes in the directions toward positive galactic longitude, toward the Sun, and toward the North Galactic Pole, respectively.

### 5.3.3 50 kmC

The location of 50 kmC is more complicated, because its LV ridge overlaps with those of Arms II, III, V and the far-side 3 kpc expanding ring (Dame & Thaddeus 2008), and the proximity on the sky suggests association with Sgr A. Adopting the kinetic energy ($\sim 7 \times 10^{49}$ erg), velocity dispersion ($\sigma_v \sim 28$ km s$^{-1}$), and mean gas density ($\sim 10^4$ H$_2$ cm$^{-3}$) derived by Tsuboi, Miyazaki, and Okumura (2009), we estimate the molecular mass to be $M_{\rm mol} \sim 10^4\, M_\odot$. This mass is two orders of magnitude smaller than the dynamical mass of $M_{\rm dyn} \sim 3\sigma_v^2 r/G \sim 10^6\, M_\odot$ for $r \sim 1$ pc, and therefore 50 kmC is not an isolated bound "cloud" but an expanding shell or an arm orbiting (streaming) in the Galactic potential.

For detailed inspection of kinematics we present CS ($J = 2$–1) LVDs and a moment-0 map in figures 16 and 17. The three components of 50 kmC, clump A (north-west), B (center), and C (south-east) (Tsuboi et al. 2009), are resolved, and reveal LV ridges coherently inclined with velocity gradients equal to that of Arm V. It is also stressed that the clumps have large velocity widths of $2\sigma_v \sim 50$–60 km s$^{-1}$.

As to the location of 50 kmC, we consider the following three possibilities, while we rule out Arm II and the far 3 kpc ring because they are on the opposite side of Sgr A:

(i) 50 kmC is located near Sgr A because of their proximity on the sky (Tsuboi et al. 2009). The large velocity width is attributed to expansion of a supernova remnant. However, the velocity gradient has not been discussed. The 3D position of the cloud center with respect to Sgr A* is approximately $(x^*, y^*, z^*) \sim (5.6, 0, -3.4)$ (pc).

(ii) 50 kmC is part of Arm V, because the LVD exactly overlaps with Arm V and the velocity gradient is equal to that of Arm V. Also, the large velocity width is explained by the Galactic rotation. This model puts the cloud center at $(x^*, y^*, z^*) \sim (5.6, 7.7, -3.4)$ (pc).

(iii) 50 kmC is part of Arm III, because the LVDs approximately overlap with each other. This assumes $(x^*, y^*, z^*) \sim (5.6, 42, -3.4)$ (pc). However, the velocity gradient and the large velocity width are not explained.

We here consider that the second scenario is plausible, but the possibilities of (i) and (iii) cannot currently be ruled out.

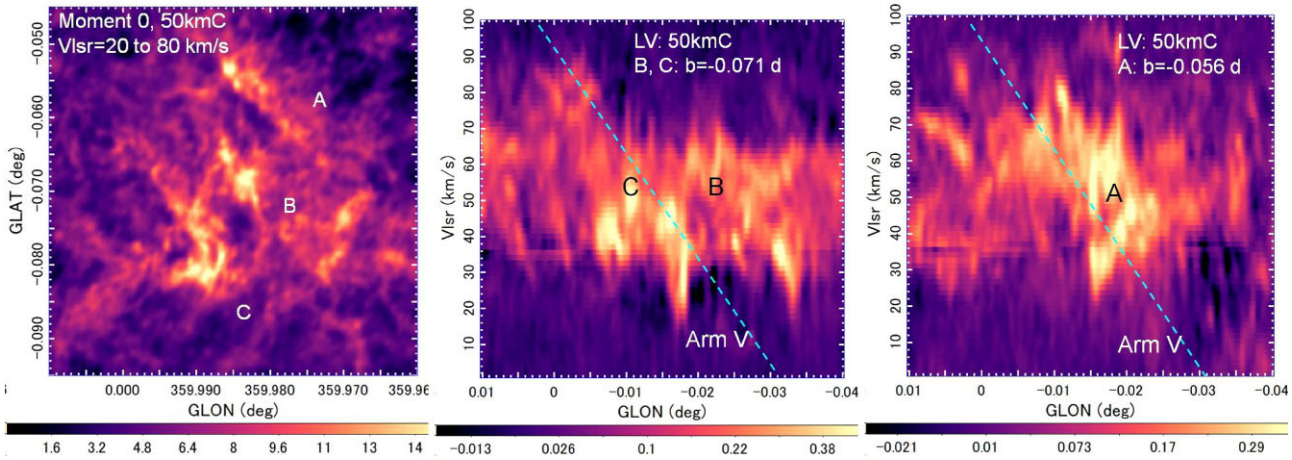


**Fig. 17.** [Top] Moment-0 map of 50 kmC in CS ($J = 2$–1) integrated from $v_{LSR} = 20$ to 80 km s$^{-1}$ (intensity scale in km s$^{-1}$ Jy beam$^{-1}$). The cloud is composed of three sub-clouds A, B, and C, which do not appear in the masked moment maps in figure 10. [Middle] LVD at $b = -0.^{\circ}071$ across 50 kmC-B and C (intensity scale in Jy beam$^{-1}$). The dashed line is the extension of Arm V. [Bottom] Same, but at $b = -0.^{\circ}056$ across 50 kmC-A.

### 5.4 200 pc expanding molecular ring (EMR)

In addition to the main structures of the CMZ like the GC arms, figures 1–7 also exhibit more complicated features surrounding these. One such feature is the expanding molecular ring commonly appearing in these LVDs, marked in figure 7 by the nearly horizontal dashed lines EMR+ and EMR−. It has long been debated whether the EMR is due to an expanding ring caused by an explosion at the center (Kaifu et al. 1972; Scoville 1972; Sofue 2017), or a "parallelogram" due to non-circular gas flow in a bar potential (Binney et al. 1991; Sormani et al. 2015; Tress et al. 2020).

Discussion of these features is beyond the scope of this paper, but we point out that the EMR is fainter than the main Arms I and II by a factor of $\sim 10^{-2}$ in the surface brightness of the molecular lines, and the total mass is an order of magnitude smaller than that of the CMZ (Sofue 2017). Furthermore, the EMR has a large vertical extension above and below the CMZ of $\sim \pm 100$ pc, which deviates significantly from the vertical extent–radius relation in figure 12. Therefore, in order for the EMR (parallelogram) to act as a mass supplier to the CMZ, the gas transported from the outer Galactic disk with a thickness of ∼20–30 pc must first be lifted to that height and then quickly compressed to the CMZ of thickness ∼10–20 pc. In this context, it has recently been argued that the western wing of the EMR may be a high-velocity ($\sim \pm 100$–200 km s$^{-1}$) and high-altitude ($z/2 \sim$ 20–60 pc) molecular inflow with a length of ∼200 pc, which acts to transport the gas into the CMZ (Veena et al. 2024).

## 6 Summary

Analyzing the molecular-line cubes of the Galactic Center taken with ALMA [CS ($J = 2$–1) and H$^{13}$CN ($J = 1$–0)], the Nobeyama 45 m telescope [$^{13}$CO ($J = 1$–0)], and the ASTE 10 m telescope [HCN ($J = 4$–3)], we have studied the kinematic behavior of GC Arms I to VI identified in the longitude–velocity diagrams (LVDs). The galactocentric radii of the arms are determined by the $dv/dl$ method assuming a flat rotation curve. Applying the LV-masking method, we also obtained moment-0 maps integrated in the velocity range within $\pm \sim 7.5$–10 km s$^{-1}$ from the LV ridges of the arms. We find that the radius of the $N$th arm is approximately given by $R \sim 630 \times 0.40^N$ pc, suggesting a logarithmic spiral or Bode's law-like discreteness of the orbits. If we consider the mini-spirals to constitute Arm VII, the relation holds from $N = 1$ (I) to 7 (VII). The vertical full extent of the arms is approximated by $z \sim 0.7(R/1\ \mathrm{pc})^{0.7}$ pc.

Unifying the derived parameters of the arms and rings, we summarize the results in figure 13 as a schematic view of the warping CMZ: Arms I and II share most of the mass (volume) of CMZ; the inner arms share a few percent of the CMZ mass (volume); hence the accretion is slow; the vertical extent of the disk decreases toward the center; and the warping amplitude or the arm's tilt from the Galactic plane increases toward the center.

## Conflict of interest

The authors declare that there is no conflict of interest.

## Data availability

The single-dish data underlying this article are available at ⟨https://www.nro.nao.ac.jp/~nro45mrt/html/results/data.html⟩. The interferometer data were taken from the internal release version of the 12 m + 7 m + TP (total power)-mode data from the ALMA cycle 8 Large Program "ALMA Central Molecular Zone Exploration Survey" (ACES, 2021.1.00172.L).

## Acknowledgments

This paper makes use of the following ALMA data: ADS/JAO.ALMA#2021.1.00172. ALMA is a partnership of ESO (representing its member states), NSF (USA), and NINS (Japan), together with NRC (Canada), NSTC and ASIAA (Taiwan), and KASI (Republic of Korea), in cooperation with the Republic of Chile. The Joint ALMA Observatory is operated by ESO, AUI/NRAO, and NAOJ.

The data analysis in this paper was partially performed at the Astronomical Data Center of the National Astronomical Observatories of Japan.

CB gratefully acknowledges funding from the National Science Foundation under Award Nos. 2108938, 2206510, and CAREER 2145689, as well as from the National Aeronautics and Space Administration through the Astrophysics Data Analysis Program under Award "3-D MC: Mapping Circumnuclear Molecular Clouds from X-ray to Radio," Grant No. 80NSSC22K1125.

COOL Research DAO (Chevance et al. 2025) is a Decentralised Autonomous Organisation supporting research in astrophysics aimed at uncovering our cosmic origins.

JMDK gratefully acknowledges funding from the European Research Council (ERC) under the European Union's Horizon 2020 research and innovation programme via the ERC Starting Grant MUSTANG (grant agreement number 714907).

KK acknowledges the supports by JSPS KAKENHI Grant Numbers JP23K20035 and JP24H00004. KMD acknowledges support from the European Research Council (ERC) Advanced Grant MOPPEX 833460.vii.

KMD acknowledges support from the European Research Council (ERC) Advanced Grant MOPPEX 833460.vii.

LC, VMR, and IJ-S acknowledge support from the grant PID2022-136814NB-I00 by the Spanish Ministry of Science, Innovation and Universities/State Agency of Research MICIU/AEI/10.13039/501100011033 and by ERDF, UE.

V MR also acknowledges support from the grant RYC2020-029387-I funded by MICIU/AEI/10.13039/501100011033 and by "ESF, Investing in your future", from the Consejo Superior de Investigaciones Científicas (CSIC) and the Centro de Astrobiología (CAB) through the project 20225AT015 (Proyectos intramurales especiales del CSIC); and from the grant CNS2023-144464 funded by MICIU/AEI/10.13039/501100011033 and by "European Union NextGenerationEU/PRTR."

IJ-S acknowledges support from ERC grant OPENS, GA No. 101125858, funded by the European Union. Views and opinions expressed are however those of the author(s) only and do not necessarily reflect those of the European Union or the European Research Council Executive Agency. Neither the European Union nor the granting authority can be held responsible for them.

PG is sponsored by the Chinese Academy of Sciences (CAS), through a grant to the CAS South America Center for Astronomy (CASSACA).

RSK thanks the 2024/25 Class of Radcliffe Fellows for highly interesting and stimulating discussions, financial support from the European Research Council via ERC Synergy Grant "ECOGAL" (project ID 855130), the German Excellence Strategy via (EXC 2181 - 390900948) "STRUCTURES," the German Ministry for Economic Affairs and Climate Action in project "MAINN" (funding ID 50OO2206), the Ministry of Science, Research and the Arts of the State of Baden-Württemberg through bwHPC and the German Science Foundation through grants INST 35/1134-1 FUGG and 35/1597-1 FUGG, and also for data storage at SDS@hd funded through grants INST 35/1314-1 FUGG and INST 35/1503-1 FUGG.

DR-V acknowledges the financial support of DIDULS/ULS, through the project PAAI 2023.

JW gratefully acknowledges funding from the National Science Foundation under Award Nos. 2108938 and 2206 510.

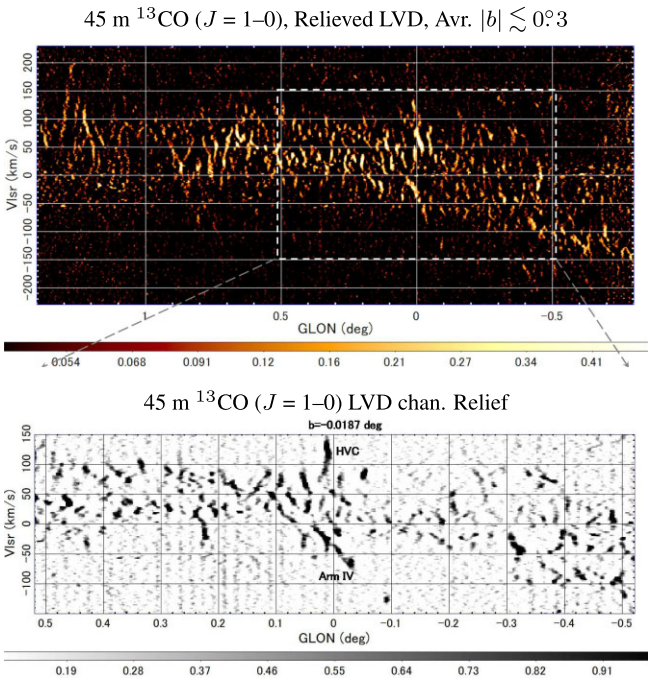


**Fig. 18.** $^{13}$CO ($J$ = 1–0) IMSHIFT-relieved LVDs in the CMZ in the $^{13}$CO ($J$ = 1–0) line observed with the 45 m telescope in the whole area (top) and the central region at $b = -0.^{\circ}02$ (bottom).

## Appendix 1. IMSHIFT-relieving method

In order to abstract tilted LV stripes representing rotating arms in the CMZ using single-dish observations, we apply the IMSHIFT-relieving technique, which is a modification of the "background-filtering" (BGF) (pressing) method (Sofue 1993). This method subtracts extended components with scale sizes greater than a threshold value (here five pixels) in one direction (here in galactic longitude), so that it enhances oblique and vertical LV stripes. This method, therefore, suppresses the horizontal LV stripes (contamination) due to the fore- and background Galactic disk. We confirmed that there are no significant differences in the results when the relieving size is from $\delta x \sim 3$ to 10 pix. Figure 18 shows an example of relieved LVDs averaged in $|b| \lesssim 0.^{\circ}3$ in the whole CMZ in the $^{13}$CO ($J$ = 1–0) line; the bottom panel is an enlargement of the central region at a fixed latitude.

The method consists of the following procedure. Let the original map represent the intensity distribution $T(x, y)$. The relieved intensity is defined by

$$\Delta T(x, y) = (\Delta T^{+} + \Delta T^{-})/2 \tag{A1}$$

where $\Delta T^{+} = T(x, y) - T(x + \delta x, y)$ and $\Delta T^{-} = T(x, y) - T(x - \delta x, y)$. We then replace the pixel values with zero, if $\Delta T < 0$. In the present analysis, we adopt a relieving size of $\delta x = 5$ pix $\sim 37.''5 = 1.5$ pc in the longitude direction. However, the following point may be kept in mind when using it: The method suppresses structures wider than the threshold width, so the obtained LVDs are not useful for discussions of large-scale arms and rings, particularly in the outer CMZ.

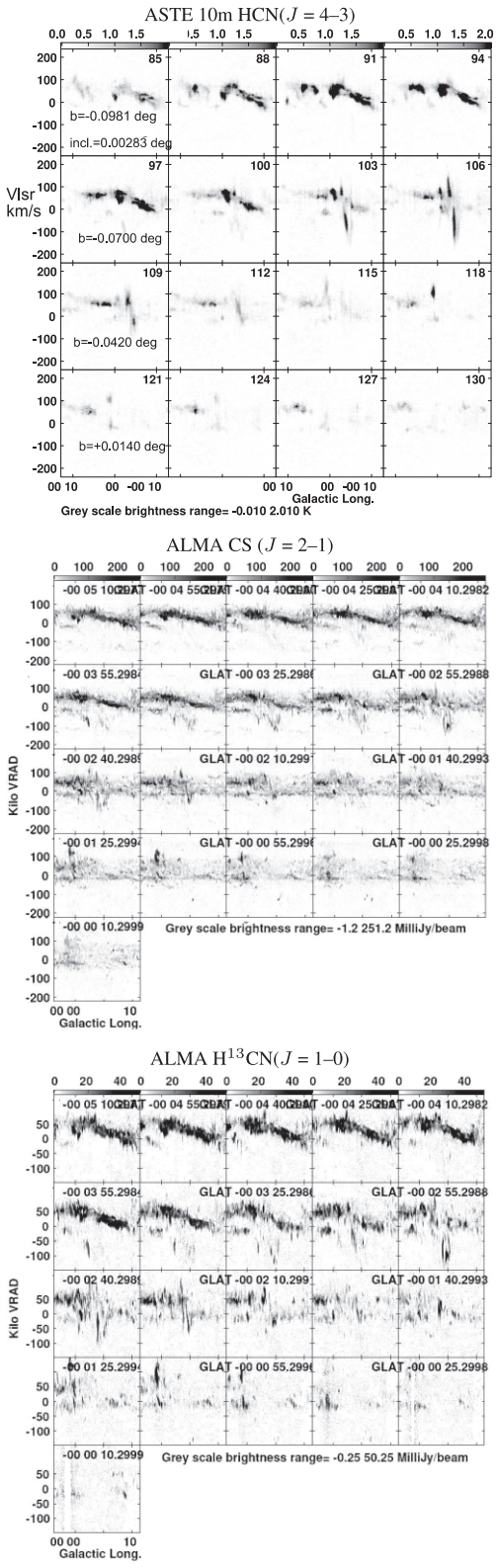


**Fig. 19.** [Top] Channel LVDs in HCN ($J$ = 4–3) by the ASTE 10 m telescope. [Middle] ACES latitude-channel maps of LVDs in CS ($J$ = 2–1) (top) and [bottom] $H^{13}CN$ ($J$ = 1–0) (bottom) of the central ±0.°12 about Sgr A*.

## Appendix 2. Channel LVDs

We present latitudinal channel maps of LVDs of the central $l \sim \pm 0.^{\circ}2$ region in the $H^{13}CN$ ($J$ = 1–0) line from ASTE 10 m in the top panel of figure 19 in order to present high-density LV arms. The second and bottom panels show CS ($J$ = 2–1) and $H^{13}CN$ ($J$ = 1–0) line channel LVDs from ACES of the central $\sim \pm 0.^{\circ}1$ region at higher resolutions, respectively. These figures along with the original cubes were used to find and identify an arm as a straight LV ridge extending over ∼100 km $s^{-1}$, and to confirm that the arm is not an artifact specific to a certain channel but a real object by comparing the feature with those continuously appearing in the neighboring multiple channels.

## References

Bally, J., Stark, A. A., Wilson, R. W., & Henkel, C. 1987, ApJS, 65, 13
Bally, J., Stark, A. A., Wilson, R. W., & Henkel, C. 1988, ApJ, 324, 223
Battersby, C., et al. 2020, ApJS, 249, 35
Battersby, C., et al. 2025, ApJ, 984, 157
Binney, J., Gerhard, O. E., Stark, A. A., Bally, J., & Uchida, K. I. 1991, MNRAS, 252, 210
Chevance, M., Kruijssen, J. M. D., & Longmore, S. N. 2025, arXiv:2501.13160
Dame, T. M., & Thaddeus, P. 2008, ApJ, 683, L143
Etxaluze, M., Smith, H. A., Tolls, V., Stark, A. A., & González-Alfonso, E. 2011, AJ, 142, 134
Feldmeier, A., et al. 2014, A&A, 570, A2
Genzel, R., Stacey, G. J., Harris, A. I., Townes, C. H., Geis, N., Graf, U. U., Poglitsch, A., & Stutzki, J. 1990, ApJ, 356, 160
Ginsburg, A., et al. 2023, ApJ, 959, 36
GRAVITY Collaboration 2019, A&A, 625, L10
Guzmán, A. E., Sanhueza, P., Contreras, Y., Smith, H. A., Jackson, J. M., Hoq, S., & Rathborne, J. M. 2015, ApJ, 815, 130
Henshaw, J. D., et al. 2016, MNRAS, 457, 2675
Henshaw, J. D., et al. 2019, MNRAS, 485, 2457
Henshaw, J. D., Barnes, A. T., Battersby, C., Ginsburg, A., Sormani, M. C., & Walker, D. L. 2023, ASP Conf. Ser., 534, 83
Herrnstein, R. M., & Ho, P. T. P. 2005, ApJ, 620, 287
Heywood, I., et al. 2022, ApJ, 925, 165
Hsieh, P.-Y., et al. 2021, ApJ, 913, 94
Iwata, Y., Oka, T., Takekawa, S., Tsujimoto, S., & Enokiya, R. 2023, ApJ, 950, 25
Kaifu, N., Kato, T., & Iguchi, T. 1972, Nat. Phys. Sci., 238, 105
Kim, W.-T., & Stone, J. M. 2012, ApJ, 751, 124
Kruijssen, J. M. D., et al. 2019, MNRAS, 484, 5734
Kruijssen, J. M. D., Dale, J. E., & Longmore, S. N. 2015, MNRAS, 447, 1059
Krumholz, M. R., & Kruijssen, J. M. D. 2015, MNRAS, 453, 739
Krumholz, M. R., Kruijssen, J. M. D., & Crocker, R. M. 2017, MNRAS, 466, 1213
Lipman, D., et al. 2025, ApJ, 984, 159
Lu, X., et al. 2024, ApJ, 962, 39
Martín, S., Martín-Pintado, J., Montero-Castaño, M., Ho, P. T. P., & Blundell, R. 2012, A&A, 539, A29
McClure-Griffiths, N. M., Dickey, J. M., Gaensler, B. M., Green, A. J., Green, J. A., & Haverkorn, M. 2012, ApJS, 199, 12
Mills, E. A. C., Togi, A., & Kaufman, M. 2017, ApJ, 850, 192
Molinari, S., et al. 2011, ApJ, 735, L33
Montero-Castaño, M., Herrnstein, R. M., & Ho, P. T. P. 2009, ApJ, 695, 1477

Morris, M., & Serabyn, E. 1996, ARA&A, 34, 645
Nogueras-Lara, F. 2022, A&A, 668, L8
Nogueras-Lara, F., Schödel, R., Neumayer, N., & Schultheis, M. 2021, A&A, 647, L6
Oka, T., Hasegawa, T., Sato, F., Tsuboi, M., & Miyazaki, A. 1998, ApJS, 118, 455
Oka, T., Nagai, M., Kamegai, K., & Tanaka, K. 2011, ApJ, 732, 120
Oka, T., White, G. J., Hasegawa, T., Sato, F., Tsuboi, M., & Miyazaki, A. 1999, ApJ, 515, 249
Petkova, M. A., et al. 2023, MNRAS, 525, 962
Ridley, M. G. L., Sormani, M. C., Treß, R. G., Magorrian, J., & Klessen, R. S. 2017, MNRAS, 469, 2251
Rodriguez-Fernandez, N. J., & Combes, F. 2008, A&A, 489, 115
Sánchez-Monge, Á., Schilke, P., Ginsburg, A., Cesaroni, R., & Schmiedeke, A. 2018, A&A, 609, A101
Sawada, T., Hasegawa, T., Handa, T., & Cohen, R. J. 2004, MNRAS, 349, 1167
Scoville, N. Z. 1972, ApJ, 175, L127
Shibata, K., & Uchida, Y. 1986, PASJ, 38, 631
Shirley, Y. L. 2015, PASP, 127, 299
Sofue, Y. 1993, PASP, 105, 308
Sofue, Y. 1995, PASJ, 47, 527
Sofue, Y. 2006, PASJ, 58, 335
Sofue, Y. 2017, MNRAS, 470, 1982
Sofue, Y. 2022, MNRAS, 516, 907
Sofue, Y. 2024, PASJ, 76, 773
Sormani, M. C., et al. 2019, MNRAS, 488, 4663
Sormani, M. C., Binney, J., & Magorrian, J. 2015, MNRAS, 449, 2421
Sormani, M. C., Tress, R. G., Glover, S. C. O., Klessen, R. S., Battersby, C. D., Clark, P. C., Hatchfield, H. P., & Smith, R. J. 2020, MNRAS, 497, 5024
Stolovy, S., et al. 2006, J. Phys. Conf. Ser., 54, 176
Takekawa, S., Oka, T., & Tanaka, K. 2017, ApJ, 834, 121
Tanaka, K., Nagai, M., Kamegai, K., Iino, T., & Sakai, T. 2018, ApJS, 236, 40
Tokuyama, S., Oka, T., Takekawa, S., Iwata, Y., Tsujimoto, S., Yamada, M., Furusawa, M., & Nomura, M. 2019, PASJ, 71, S19
Tress, R. G., Sormani, M. C., Glover, S. C. O., Klessen, R. S., Battersby, C. D., Clark, P. C., Hatchfield, H. P., & Smith, R. J. 2020, MNRAS, 499, 4455
Tsuboi, M., Handa, T., & Ukita, N. 1999, ApJS, 120, 1
Tsuboi, M., Kitamura, Y., Uehara, K., Miyawaki, R., Tsutsumi, T., Miyazaki, A., & Miyoshi, M. 2017, ApJ, 842, 94
Tsuboi, M., Kitamura, Y., Uehara, K., Tsutsumi, T., Miyawaki, R., Miyoshi, M., & Miyazaki, A. 2018, PASJ, 70, 85
Tsuboi, M., Miyazaki, A., & Okumura, S. K. 2009, PASJ, 61, 29
Uehara, K., Tsuboi, M., Kitamura, Y., Miyawaki, R., & Miyazaki, A. 2019, ApJ, 872, 121
Veena, V. S., et al. 2024, A&A, 689, A121
Wada, K., Baba, J., & Saitoh, T. R. 2011, ApJ, 735, 1
Walker, D. L., et al. 2021, MNRAS, 503, 77
Walker, D. L., et al. 2025, ApJ, 984, 158
Wright, M. C. H., Coil, A. L., McGary, R. S., Ho, P. T. P., & Harris, A. I. 2001, ApJ, 551, 254
Yan, Q.-Z., et al. 2017, MNRAS, 471, 2523
Zhao, J.-H., Morris, M. R., Goss, W. M., & An, T. 2009, ApJ, 699, 186



Received: 2024 November 7; Accepted: 2025 March 25